UCLA
UCLA Electronic Theses and Dissertations

Title

Incorporating Metal-Organic Frameworks into Graphene-Based Electrodes for High-Performance Capacitive Energy Storage

Permalink

https://escholarship.org/uc/item/9j59b4nw

Author

Chen, Amylynn C.

Publication Date

2016

Peer reviewed|Thesis/dissertation

UNIVERSITY OF CALIFORNIA

Los Angeles

Incorporating Metal-Organic Frameworks into Graphene-Based Electrodes

for High-Performance Capacitive Energy Storage

A thesis submitted in partial satisfaction

of the requirements for the degree Master of Science

in Chemistry

by

Amylynn C. Chen

2016

ABSTRACT OF THE THESIS

Incorporating Metal-Organic Frameworks into Graphene-Based Electrodes

for High-Performance Capacitive Energy Storage

by

Amylynn C. Chen

Mater of Science in Chemistry

University of California, Los Angeles, 2016

Professor Richard B. Kaner, Chair

The high porosity and openness of metal-organic frameworks (MOFs) have been extensively studied in gas adsorption, catalysis, and the use as templates for nanoporous materials synthesis; but its potential in electrochemical energy storage is not well understood. MOFs consist of redox active metal clusters and tunable pore size, which enable the ability to contribute to pseudocapacitance in electrochemical supercapacitors. Although MOFs are generally considered as poor conductors, doping MOFs with highly conductive graphene sheets can potentially enhance the capacitance in pure graphene capacitive devices. In this study, a four-metal MOF-74 (M4M-MOF-74) was selected to investigate the capacitance enhancement due to its unique coordinately unsaturated metal sites. The MOF-74 bears one-dimensional channels that can adsorb H^+ and Li^+ very well, but not Na^+ in aqueous electrolytes, allowing ions of appropriate

size to access the framework and to fully interact with the metal sites. Moreover, the MOF/graphene hybrid electrodes demonstrate great conductivity, high areal capacitance, and good stability in an H_2SO_4 aqueous electrolyte. At a scan rate of 10 mV/s, the hybrid electrode exhibits a high areal capacitance of 54.1 mF/cm^2, which is about four times higher than a pure graphene electrode. This work could potentially open up a new application for MOFs in electrochemical capacitors.

The thesis of Amylynn C. Chen is approved.

Joseph Ambrose Loo

Alexander Michael Spokoyny

Richard B. Kaner, Committee Chair

University of California, Los Angeles

2016

DEDICATION

I dedicate this work to my mom for her love and sacrifice.

TABLE OF CONTENTS

TABLE OF FIGURES

ACKNOWLEDGEMENTS

Chapter 1: Introduction

As the demands on electric automobiles rise, the production of batteries increases along with environmental concerns. The development of electrical energy storage devices has been widely studied during the past decades to meet public and environmental needs. Many renewable sources are currently used to produce energy, but it is critical for the energy generated to be properly transferred and stored; that's where batteries and electrochemical capacitors come into play.

1.1 Supercapacitors

Supercapacitors, also known as electrochemical capacitors (ECs), advance the functionalities of capacitors, which can be employed as primary building blocks in various types of circuits, from portable electronics to large-scale power supplies.[1] In comparison to batteries, ECs have much faster charge to discharge rates, higher capacitance, and longer cycle life. To exceed the capability of standard batteries, ECs are designed using porous and electrochemically stable electrode materials with high accessible surface areas, such as activated carbons, carbon nanotubes, and graphene.

One of the most promising applications of electrochemical capacitors is in electric vehicles, such as urban buses which have frequent stops, determined routes, and limited travel distance.[3] Sinautec Automobile Technologies and Shanghai Aowei Technology Corporation together developed a series of ECs powered electric buses, which have served Shanghai since 2006. The bus only requires 30 seconds of recharging time at each bus stop, can travel a maximum distance of 3.5 miles, and uses less than 20% of the fuel cost of a conventional bus.[2] To generate the operational energy (5.9 kWh), numerous carbon-based supercapacitors are connected in parallel

which contribute to the bus weight of 13 tons.[2] In order to incorporate supercapacitors into a wider range of applications it is clear that a more compact and efficient electrical storage design is required.

1.2 Graphene

The two-dimensional material graphene was brought to the world's attention in 2010 when its discoverers won the Nobel Prize in Physics. Graphene is a single layer of carbon atoms tightly packed in a hexagonal lattice. The sp^2-hybridized orbitals of the carbons in plane are responsible for binding and the high intrinsic mobility of $2*10^5$ cm^2 V^{-1} s^{-1}.[4] Besides high conductivity, another key factor to the energy storage capacity of a supercapacitor is the surface area of its electrode material. Graphene is known as a high surface area and high porosity material; the theoretical limit for the surface area of graphene is 2630 m^2/g,[5] however, measured values are often considerably lower, e.g. 1520 m^2/g.[6] Although the tendency of sheet restacking is inevitable, which sacrifices specific surface area, graphene still has superior conductivity and capacitance when compared to active carbon used in commercial carbon-based supercapacitors.[7] Also, comparing it to the highly conductive carbon nanotubes (CNTs), graphene has much higher surface area and capacitance. Additionally, graphene can be reduced from the solution-processable graphene oxide (GO) by exfoliation of graphite powder via solution oxidation, which makes the large scale production of graphene possible at a low cost.[8] Last but not least, its biodegradability allows graphene to be a sustainable alternative for new generation energy storage material.[36]

1.3 Graphene-Based Pseudocapacitors and Battery-like Capacitors

Current commercial and experimental ECs still contain limitations, including low energy densities and slow rate capabilities. In the past decade, countless efforts have been invested into improving the electrochemical performance by introducing metal oxides into the ECs electrode. Typical carbon material-based ECs (graphene, active carbons, and carbon nanotubes) function based on a double-layer charge storage mechanism, in which the charges are stored electrostatically through reversible ion adsorption from the electrolyte to the active materials.[9] In spite of some ambiguities in the definitions of the EC types, there are generally two types of EC electrode materials that utilize metal oxides to enhance the energy density. The first type is by introducing redox active species, such as $Ni(OH)_2$[10] or other materials that exhibit Faradaic behavior that is electrochemically reversible; this type of electrode is defined as a battery-type electrode.[11] The second type is referred as a pseudocapacitive electrode that describes the behavior of electrode materials, such as RuO_2[12] and MnO_2[13], that obtains a linear dependence of the charge stored with changing potential via electron-transfer mechanisms.[11] In this work, a hybrid supercapacitor is presented, which exhibits both electrostatic separation of charges and reversible Faradaic charge-transfer behavior on the electrodes.

1.4 Metal-Organic Frameworks

Metal-Organic Frameworks (MOFs) are highly porous materials that were first popularized by Yaghi and Li in 1995.[14] MOFs are crystalline coordination polymers consisting of transition metal ions or clusters and organic linkers that often contain carboxylic acid and hydroxyl groups. The clusters are stabilized by bridging ligands forming soluble complexes which self-assemble into one-, two-, or three-dimensional frameworks; the networks of clusters are supported by the

3

strong metal-ligand coordination bonds.[15] The most prominent advantage of this class of materials is that by carefully choosing the metal clusters and organic linkers, it is possible to tailor the structure, surface area, pore size and the chemical environment of the pores by design.[16] These materials have extremely low density (~ 0.13 g cm^{-3}) with outstanding pore volumes, well-defined porous structures, and tremendous surface areas (up to 10,000 m^{2}g^{-1}).[17] Because of their high porosity and structural openness, large efforts have been invested in the applications of MOFs for gas adsorption, catalysis, and the use as templates for nanoporous materials synthesis. However, its potential in electrochemical energy storage is not well understood. In comparison to nano-metal oxides, which often only have their surfaces interacting with electrolyte, the openness of MOFs could allow electrolyte to freely access the framework and interact with each metal cluster. The open structure of MOFs could directly lead to a higher capacity for ion storage. Depending on the chemical nature of the MOF, some may also undergo redox reactions quite efficiently.

1.5 Incorporation Metal-Organic Frameworks into Graphene-Based Supercapacitors

The focus of this work is to utilize the open structure and the redox species within MOFs to enhance capacitance of pure carbon material-based electrodes. However, MOFs are generally electronically insulating materials lacking long-range electronic communication because the organic linkers are insulators with little π-π conjugation. Recent studies have demonstrated some MOFs can obtain excellent electronic conductivity and high charge mobility via ligand π and metal d orbitals coupling.[18,19]
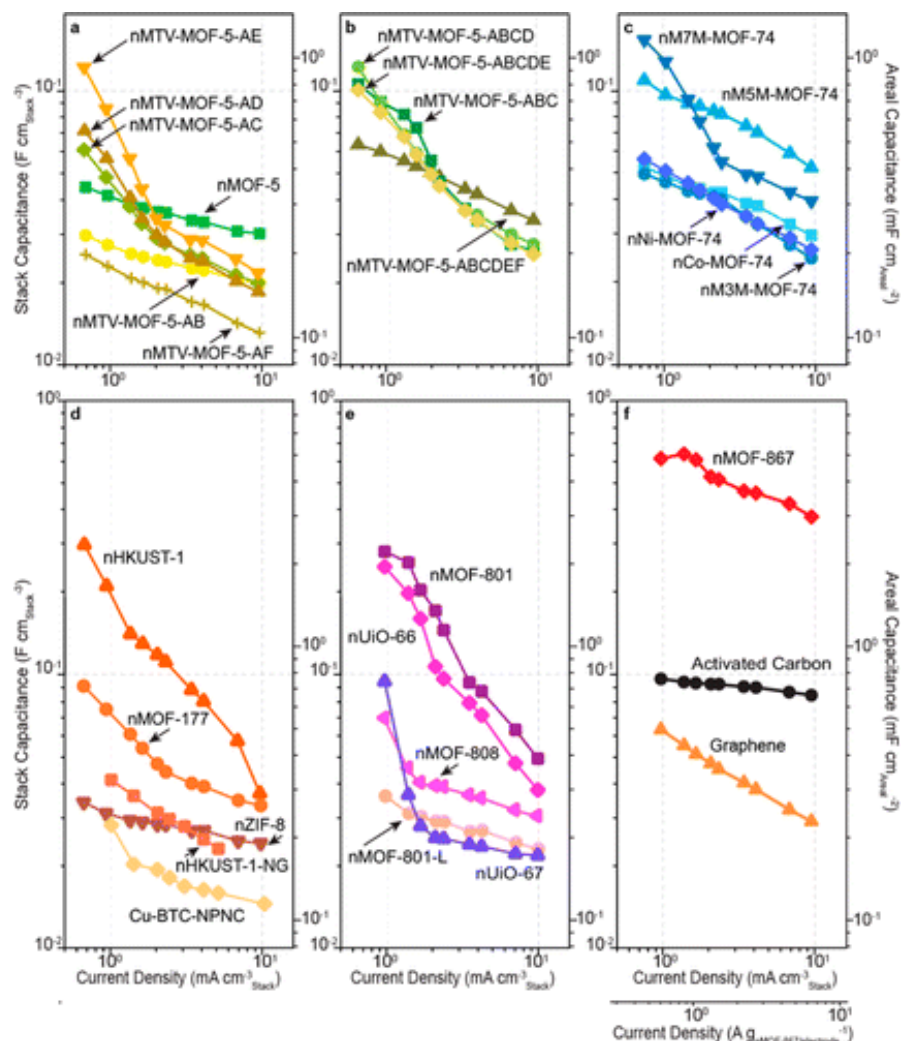
Figure 1-1. Volumetric stack and areal capacitance of nMOFs and related carbon material supercapacitors: (a) multiple nMOFs with MOF-5 structure constructed by different organic linkers and pore environments and (b) mixed functionalites; (c) several MOF-74s with mixed multimetallic metal oxide clusters; (d) various MOFs with different metal oxides comparing to nHKUST-1 electrode with nonporous, noncrystalline and no graphene constituents; (e) Zirconium (IV) MOFs with organic linkers of different lengths and shape; (f) the best performance electrode, zirconium-based nMOF-867, comparing to activated carbon and graphene. Reproduced with permission.[20]

In order to obtain highly conducting of electrodes, MOFs can be doped into graphene sheets to achieve enhanced electron mobility. In a recent study[20]; Choi et al. employed this approach and investigated a series of graphene-doped nano-MOFs (nMOFs) to fabricate symmetric supercapacitors, and found that a zirconium MOF exhibited a high stack and areal capacitance of

5

0.64 and 5.09 mF cm^{-2} at a current density of 0.88 mA cm^3. Twenty-three nMOFs with various metal clusters, organic linkers, pore sizes, crystal sizes and geometric structures, were investigated; the stack and areal capacitance of graphene-doped nMOFs electrodes as a function of current density are summarized in Figure 1-1.

There are a few key points highlighted in this study that provide critical understandings on how different properties of MOFs may effect capacitance. First, the pore environment of the MOFs can influence capacitance, which is evident from the variation in capacitance of the MOF-5 series (Figure 1-1a,b). The selected MOF-5s contain different functionalities on their organic linkers. For example, the nMTV-MOF-5-AF has large functional groups that might block the pores and cause limited ion access within the framework. As a result, this particular MOF obtains the lowest capacitance in the series. Second, mixing more than three types of metallic metal oxide units in MOF-74 gives better performance than a single metal MOF-74 (Figure 1-1c); however, the reason behind this result is not specified. Finally, out of the 23 selected MOFs, only the zirconium-based nMOF-867 exceeds the performance of commercial activated carbon. This remarkable result was explained by the sp^2 nitrogen atoms in the organic linker of nMOF-867, which enhances the interaction with ions and improves the device performance.[20]

Nonetheless, these electrodes appear to have poor capacitance retention as evidenced by the rapid capacitance drop with increasing current density, indicating poor conductivity and instability of the electrodes. Furthermore, an organic electrolyte of tetraethylammonium tetrafluoroborate, $(C_2H_5)_4NBF_4$ or TEABF$_4$, was used; this may cause instability, high cost, low conductivity, the need for a strict assembly process and limited pore accessibility due to large ion size.[35] The diameters of $(C_2H_5)_4N^+$ or TEA$^+$ and BF$_4^-$ ions are 0.68 and 0.33 nm respectively.[20] Based on a study[21] in 2008, when a cation ion TEA$^+$ enters a pore that is less than 1.5 nm in

diameter, the cation partially loses its solvent shell. This mechanism disfavors the accessibility of the electrolyte in the framework, thus resulting in insufficient charge transfer and low capacitance.
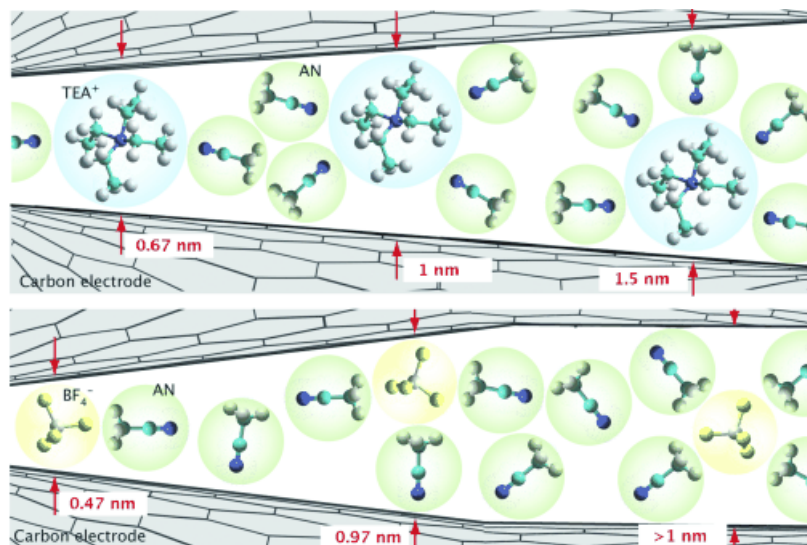
Figure 1-2. Geometric confinement of ions in small pores. With a pore size below 1.5 nm, both TEA^+ and BF_4^- ions enter the pores either bare or with partial solvent shells, where the solvent is acetonitrile (AN). Reproduced with permission.[21]

Learning from the previous study, M4M-MOF74 containing four types of metal oxide units was chosen for this work. MOF-74 is known for its ability to incorporate multiple metals without changing the structure[22], and it has one-dimensional pores of 10.8 Å.[23,24] Because of its pore size, a few aqueous electrolytes with small ion sizes, such as H_2SO_4, $LiNO_3$ and Na_2SO_4, were selected to investigate the effect of ion accessibility on capacitance. Moreover, instead of directly mixing graphene with MOFs, the electrodes were prepared by doping MOFs into graphene oxide (GO) in aqueous solution. Due to the hydrophobicity of graphene, it is difficult to produce well-disbursed MOF/graphene mixtures that are aqueous solution-processable for the fabrication of

high quality films. In contrast, the hydrophilic graphene oxide (GO) contains functional groups that are similar to the organic linkers of MOFs, which could potentially improve the interaction between MOFs and GO to obtain a more homogeneous mixture that leads to better films. Afterwards, the GO film is reduced by a laser-scribing method with detailed experimental procedures presented later in this thesis. The morphology of the films and the particle size was examined using scanning electron microscopy (SEM) and transmission electron microscopy (TEM). The crystallinity of MOF-74 in films was confirmed by X-ray powder diffraction (PXRD), and elemental analysis of the film surface was evaluated by X-ray photoelectron spectroscopy (XPS). Electrochemical measurements, such as cyclic voltammetry (CV), constant current (CC) and electrochemical impedance spectroscopy (EIS), were performed to investigate the properties of the electrodes. All results are discussed later in this thesis.

Chapter 2: Synthesis and Characterizations of M4M-MOF74

M4M-MOF-74 is comprised of 2,5-dihydroxyterephthalate (DOT) and four metal ions (zinc, cobalt, magnesium and nickel) forming a honeycombing structure conventionally referred to as MOF-74 (Fig. 2-1). As shown in Figure 2-1, all six oxygen atoms in DOT participate in metal-ligand coordination with the metal ions and create the octahedral sites. As previously mentioned, MOF-74 is known for its ability to incorporate multiple metals without changing the structure.[22] This unique property allows for toxic gas adsorption[22], CO_2 adsorption[25] and catalytic applications[26] of MOF-74 and its analogs. It is also found that a MOF-74 containing more than three types of metal oxide units in its structure has better capacitance performance than a single metal MOF-74 when doped with graphene.[20] In this work, a four-metal MOF-74 (M4M-MOF-74) was selected; the synthesis and characterization are presented in the following sections.
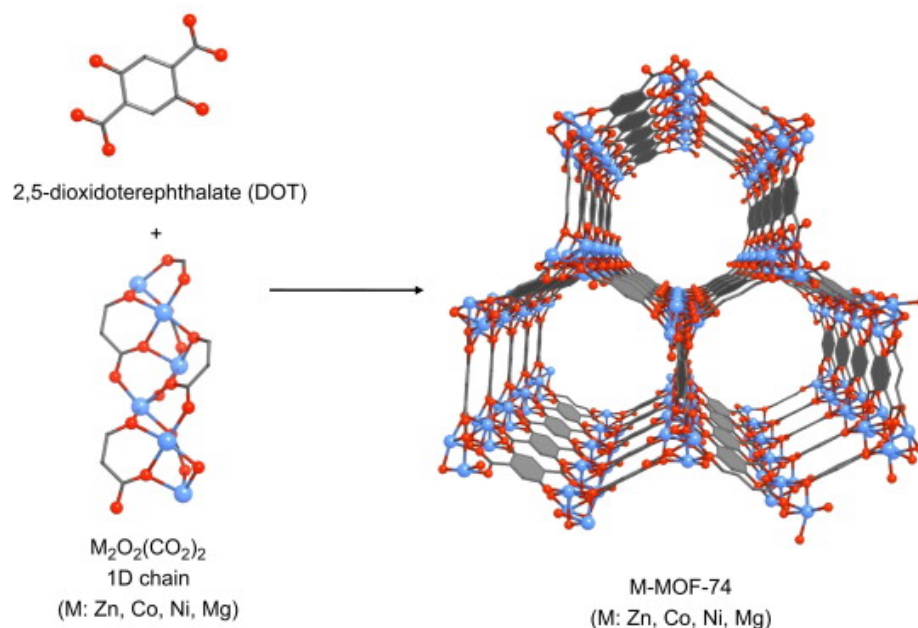
Figure 2-1. Structure of MOF-74 metal analogs. Reproduced with permission.[22]

2.1 Synthesis of M4M-MOF74

As illustrated in Figure 2-2, M4M-MOF-74 compounds were synthesized using varying amounts of metal salts ($Mg(NO_3)_2 \cdot 6H_2O$, 30.7 mg, 1.20×10^{-4} mol; $Co(NO_3)_2 \cdot 6H_2O$, 34.9 mg, 1.20×10^{-4} mol; $Ni(NO_3)_2 \cdot 6H_2O$ (34.9 mg, 1.20×10^{-4} mol; $Zn(NO_3)_2 \cdot 6H_2O$, 35.7 mg, 1.20×10^{-4} mol) dissolved with 2,5-dihydroxyterephthalic acid (H_4DOT, 30 mg, 1.5×10^{-4} mol); then, the mixture was dissolved and sonicated in DMF/EtOH/water (in a 15:1:1 ratio respectively) and heated to 120 °C for 20–24 h. After soaking and washing repeatedly with various solvents, the resulting product is an orange microcrystalline powder. The M4M-MOF-74 used in this project was synthesized by my previous mentor, Lisa Wang Ph.D.; detailed synthesis procedures are reported in her previous work[24].
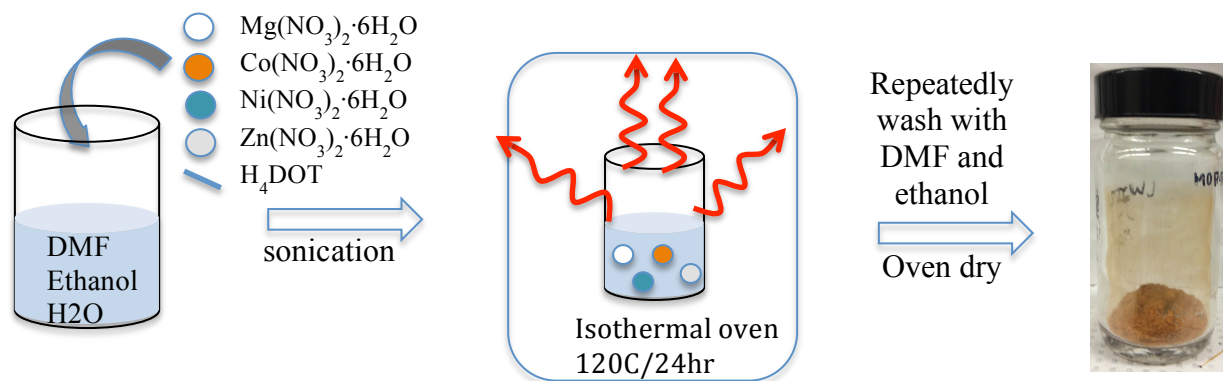
Figure 2-2. Schematic for M4M-MOF-74 Synthesis.

2.2 Characterizations of M4M-MOF-74

To confirm the crystallinity of the M4M-MOF-74, PXRD, SEM and TEM were performed prior to the electrode fabrication. All XRD patterns were collected with a Bruker AXS D8 Advance diffractometer using CuKα radiation (λ = 1.5406 Å). The PXRD pattern of M4M-MOF-74

coincides with a simulated MOF-74 PXRD pattern[24], showing the MOFs is highly crystalline (Figure 2-3). The simulated MOF-74 PXRD pattern was calculated via the software Powder Cell v.2.2.[24] Furthermore, the SEM characterization was performed using a Nova 600 SEM/FIB system, and the TEM images were collected using a Tecnai G2 TF20 TEM (FEI Inc.) operated at 200 kV. Different sizes of rod-shaped single crystals and aggregates are observed in the SEM and TEM images; single-phase morphology is seen in multiple regions of the MOF sample at different magnifications (Figures 2-4 and 2-5). In a high magnification TEM image, the metal oxide units of MOF appear as the lighter spots observed in Figure 2-5(b).
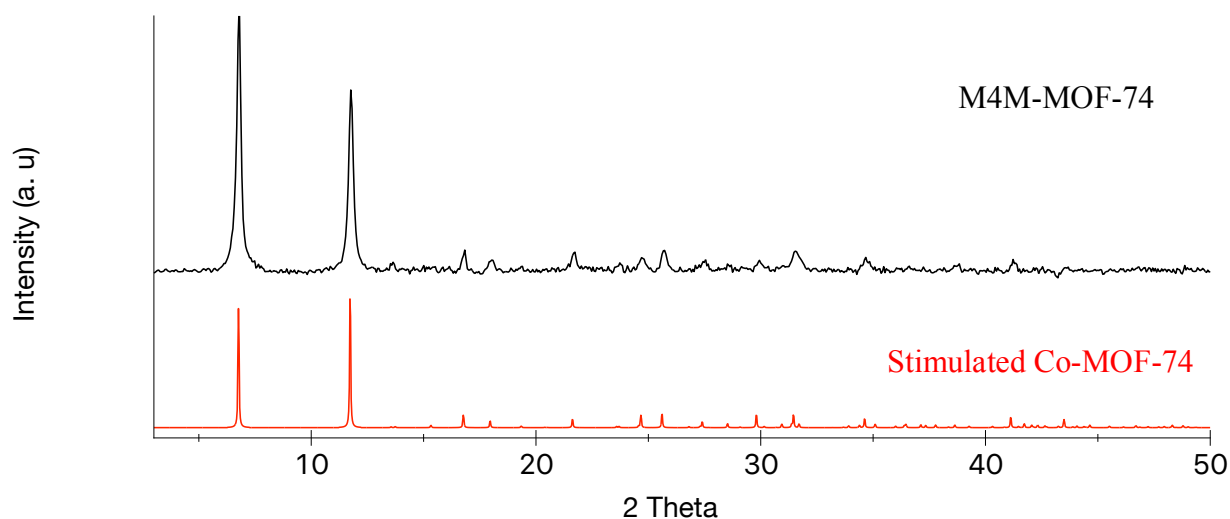
Figure 2-3. PXRD and stimulated-XRD patterns for M4M-MOF-74.

In addition, thermogravimetric analysis (TGA) and energy dispersive X-ray spectroscopy (EDS) were performed to determine the chemical composition of M4M-MOF-74. Whereas the TGA reveals the weight percentage of the coordinated water molecules, EDS mapping for elemental analysis resolves the elemental composition as $Mg_{0.190}Co_{0.612}Ni_{0.562}Zn_{0.636}(DOT)\cdot(H_2O)_{8.4}$.[24] Finally, a nitrogen adsorption measurement was conducted to examine the porosity of M4M-

11

MOF-74, which gave rise to a surface area of 900-1040 m^2/g. Detailed procedures and results of TGA, EDS, and the N_2 adsorption measurement were presented in the previous literature.[24]
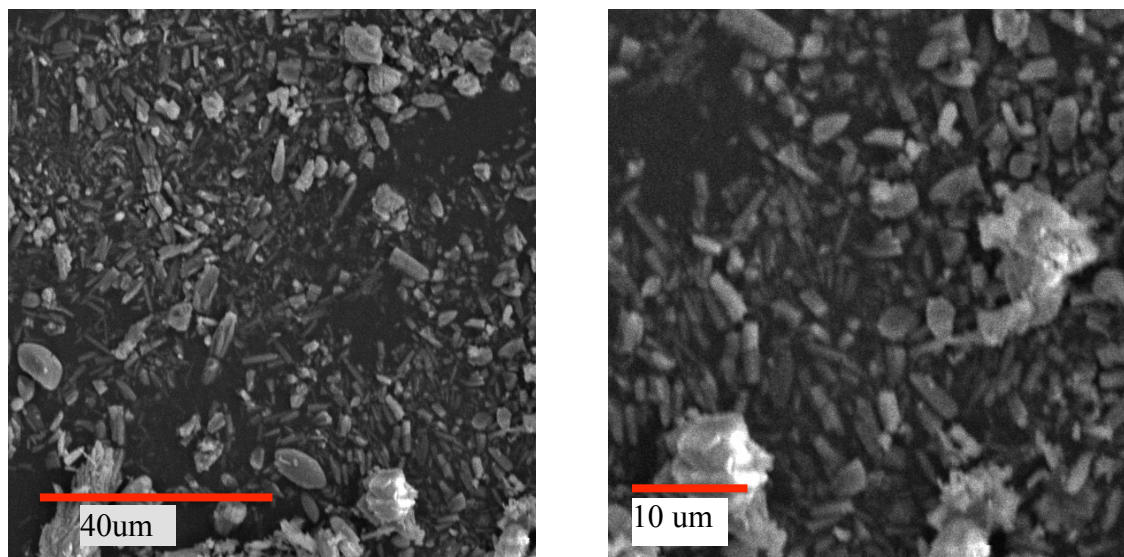
Figure 2-4. SEM images of M4M-MOF-74 at different magnifications.
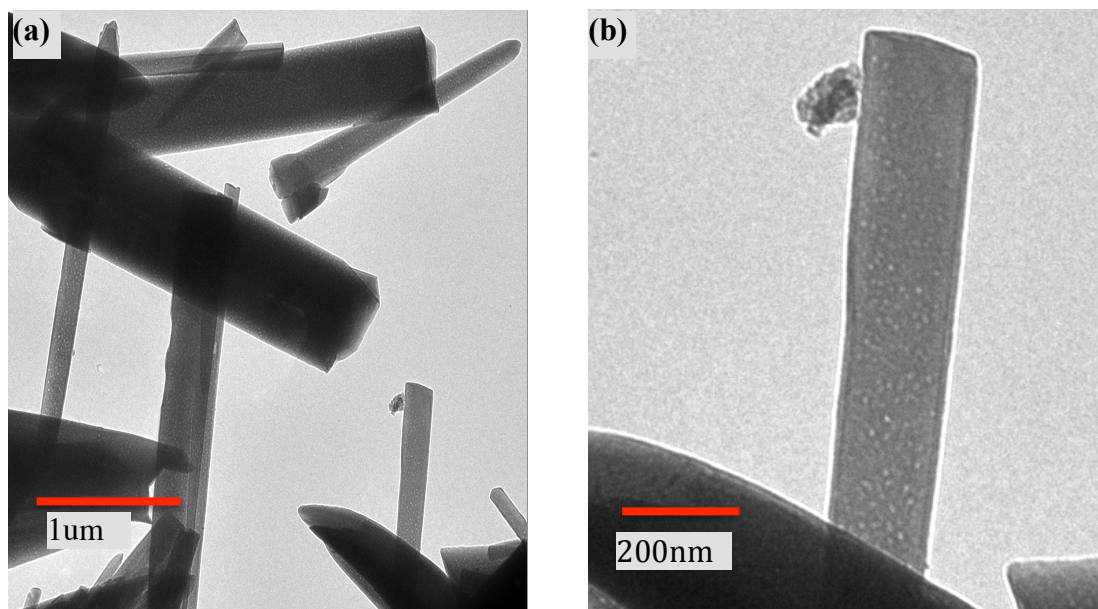
Figure 2-5. TEM images of M4M-MOF-74 at different magnifications showing single-phase morphology.

Chapter 3: Fabrication of M4M-MOF74/LSG Hybrid Electrode

It is commonly known in many GO reduction processes that graphene sheets can restack due to the strong sheet-to-sheet van der Waals interactions. This accounts for a decrease of the specific surface area of graphene that results in a lower overall capacitance. A novel laser scribing method was employed to reduce the graphene oxide (GO) films to graphene. El-Kady et al. first reported this method in 2012, where an infrared laser inside of an inexpensive commercially available LightScribe CD/DVD optical drive was used to irradiate the film.[27] As illustrated in Figure 3-1, an aqueous solution of GO is drop-cast on a flexible substrate that is attached to a regular DVD disc; then the infrared laser reduces the GO films to laser-scribed graphene (LSG). One can easily identify this transformation by observing the color of the film changing from a golden brown to black. Not only is this simple solid-state approach scalable, processible and cost-efficient, but also it can effectively avoid restacking. In Figure 3-1e, the SEM images of the film cross sections show that the initially stacked GO sheets are converted into well-exfoliated LSG sheets upon laser irradiation. Without the use of binders or current collectors, the LSG film can be directly used as EC electrodes; these electrodes obtain excellent conductivity (1738 Siemens per meter) and very high specific surface area (1520 square meters per gram).[27]

However, some intensity of the D band observed in the infrared laser-reduced graphene electrode suggests that sp^3 carbons are still present after reduction. This insufficiency in reduction could be resolved by using a higher power laser source. Therefore, in this work a higher power carbon dioxide (CO_2) laser was employed to reduce GO to LSG to improve the film quality. The fabrication and laser irradiation of the MOF/LSG electrode are described in the following sections.
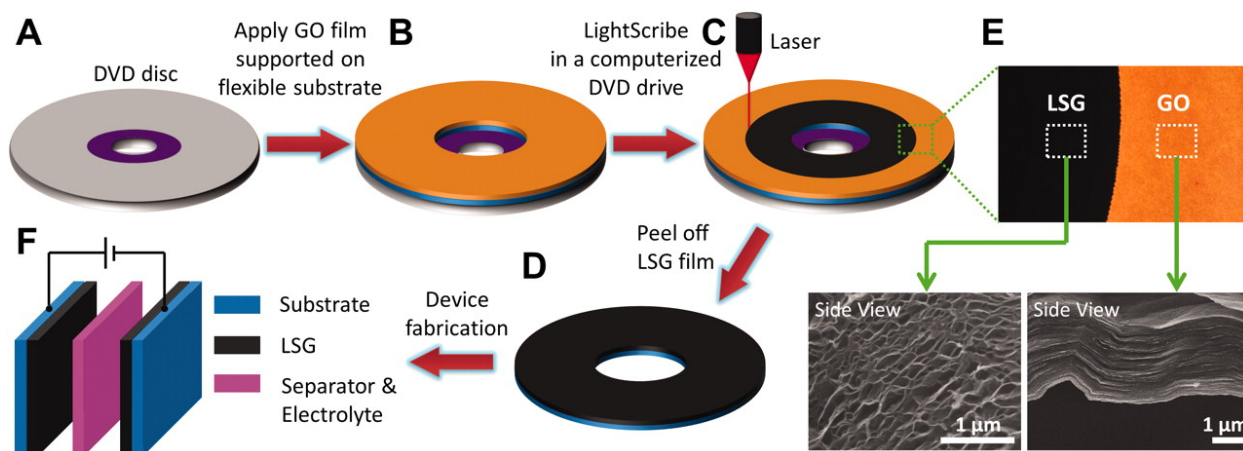
Figure 3-1. Schematic of the fabrication of laser-scribed graphene-based electrochemical capacitors. (A to D) A GO film deposited onto a flexible substrate that is attached to a DVD disc, and a computer image is then laser-scribed on the GO film inside of a LightScribe DVD drive. (E) the color of GO film changes from golden brown to black as it is reduced to laser-scribed graphene. The SEM cross-sections show the stacked GO sheets into well-exfoliated LSG film (F) A symmetric EC is constructed from two identical LSG electrodes, ion-porous separator, and electrolyte for electrochemical testing. Reproduced with permission.[27]

3.1 Thin Film of Active Material Mixture
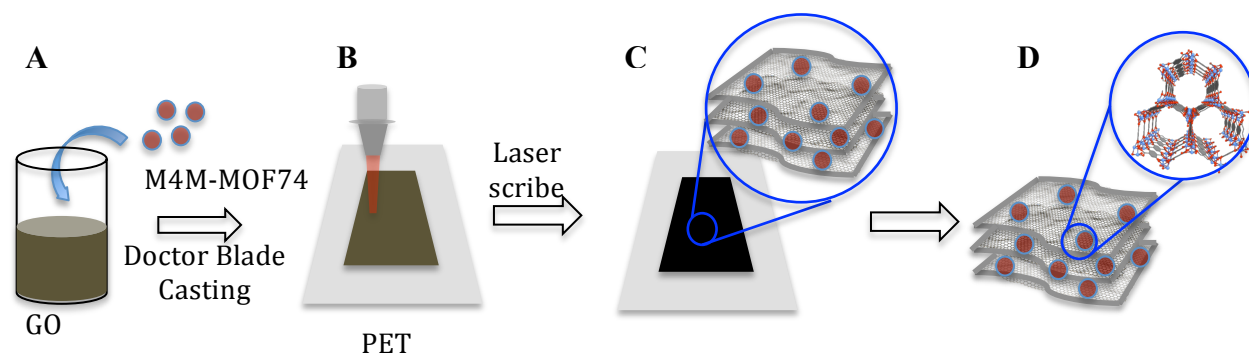
Figure 3-2. Schematic illustration of the fabrication of laser-scribed MOF-74/LSG supercapacitor electrode. (A) A well-dispersed MOF/GO solution is made by sonication and magnetic stirring; the solution is cast onto a PET film using a doctor blade. (B-D) the dried GO film is reduced by a commercially available CO_2 laser leading to a homogenous film with evenly distributed MOF particles.

The graphene oxide was synthesized by a modified Hummers method[28], and then freeze-dried using a FreeZone Freeze Dry System. 50 mg of GO powder was re-dissolved in 4 ml of

14

deionized (DI) water to obtain a brownish gray colored solution. After sonicating the solution in

an ultrasonic bath for 90 minutes at 55°C, the solution was stirred on a magnetic stirring plate for

30 min. Meanwhile, 50 mg of M4M-MOF-74 was dispersed in 1 ml of DI water by sonicating

for 20 min at 25°C and stirring for 30 min. Next, the well-dispersed GO solution was added to

the MOF solution, and afterwards the solution mixture was stirred for another 30 min (Figure 3-

2A). Then, the solution mixture was drop-cast onto a clean piece of polyethylene terephthalate

(PET) film, and a doctor blade was used to cast a 60 nm thick film (Figure 3-2B). The MOF-

74/GO film was dried overnight at room temperature; the completely dried film appeared in a

golden brown color (Figure 3-3). For the pure graphene electrode, 50 mg of GO power was re-

dissolved in 5 ml of deionized (DI) water; the solution was sonicated for 90 min at 55°C and

stirred for 30 min before casting into thin films.
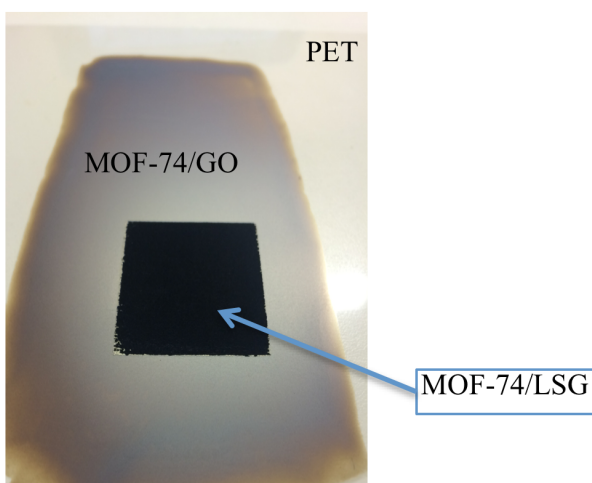
Figure 3-3. Photo of a MOF-74/GO film on a PET substrate with a laser-scribed area of 1 inch^2. The MOF-74/GO film appears golden brown, whereas the color changes to black after laser irradiation.

3.2 Carbon Dioxide Laser Scribing Reduction

A Full Spectrum H-Series desktop CO_2 Laser Engraver was used to reduce the GO film to LSG, equipped with a hobby CO_2 laser with 10.6 μm wavelength and 40 W maximum power. According to the product manual, the maximum power supplied is generally 30 to 35 watts.[29] The pre-dried film was laid flat on the honeycomb cutting table, then a program-controlled laser was used to create different shapes and images on the film. In Figure 3-4, a laser-scribed area of 1 inch^2 is shown by the color contract between the golden brown GO and the black LSG. Typically, A 3 inch^2 area can be fabricated with 16% power (~4.8 watts) and 80% speed within 5 min, and the film is uniformly reduced after only two cycles. Since the laser penetration with a selected power is constant, all the electrodes for this work were fabricated with 16% power. In this way we can experimentally control the thickness of the active material for areal capacitance measurements and comparisons.
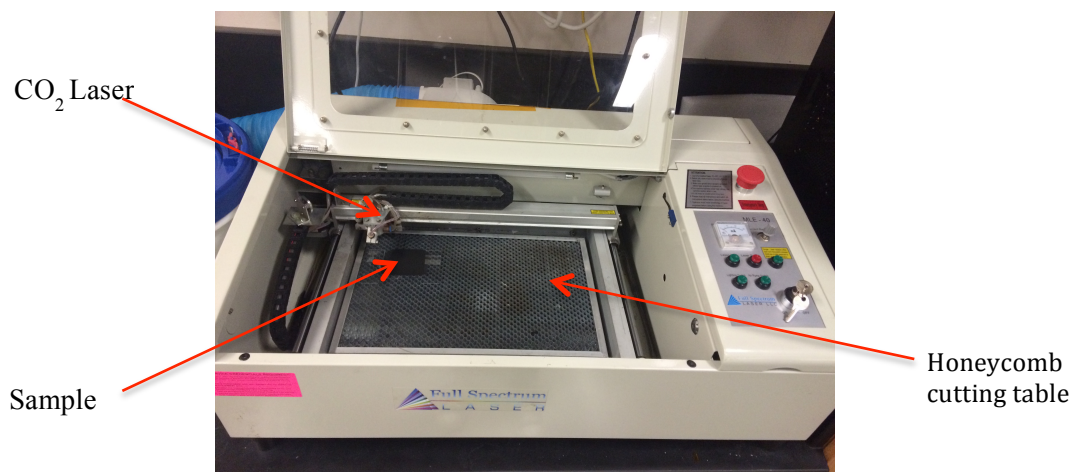
Figure 3-4. Full Spectrum H-Series desktop CO_2 laser engraver for graphene oxide reduction.

Depending on the substrate and active materials, the minimal power required for sufficient reduction varies. Exceeding the minimal reduction power can cause the top layer of graphene to

be reduced to carbon dioxide. As long as the GO film is thick enough to prevent the laser from hitting the PET substrate, the thickness of the electrode active material can still be properly controlled by this method.

Although laser scribing is a serial technique, which can limit the speed of the GO reduction, employing multiple laser sources at once can easily improve the reduction efficiency in large-scale fabrication.

Chapter 4: Characterization of M4M-MOF74/LSG Hybrid Electrode

4.1 Scanning Electron Microscopy (SEM)

Scanning electron microscopy (SEM) is a fundamental characterization method to provide high-resolution images of the sample morphology. Through bombarding a sample with an electron beam, the secondary electrons are generated to create the SEM images. These images not only reveal topographical information, but also show differences in the conductivities of materials due to charging effects. Herein, the SEM characterization of MOF-74/LSG and LSG electrodes was performed using a JEOL JSM-6700F FE-SEM system. Figures 4-1a and 4-1b show well-exfoliated laser-scribed graphene sheets with excellent conductivity at various magnifications. In comparison to the pure LSG electrode, the MOF-74/LSG electrodes show uniform distribution of MOF-74; the MOF particles appear as the bright spots allocated on the conductive LSG (Figures 4-1c and d). Generally, MOFs have poor electronic conductivity; as a result, the electrons from the SEM beam are trapped on the MOF particles. This causes the particles to charge up, and results in the brightness observed in the images. Through the charging effect, we can confirm the MOFs are uniformly doped in the LSG sheets.
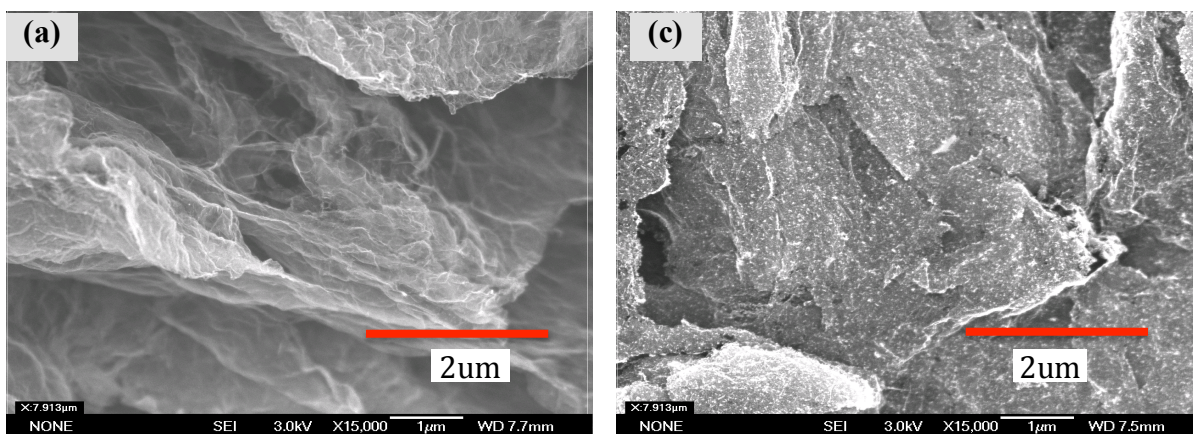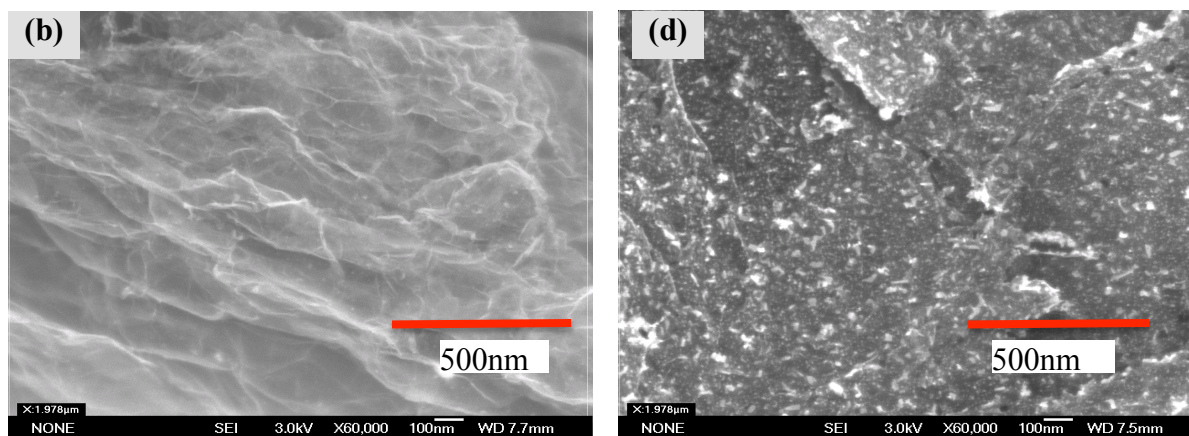
Figure 4-1. SEM images of (a-b) pure LSG and (c-d) MOF-74/LSG electrodes. Both samples were examined at 15K and 60K magnification at 3kV for comparison.

4.2 Transmission Electron Microscopy (TEM)

Transmission electron microscopy (TEM) is another fundamental microscopy technique in which a beam of electrons is transmitted through and interacts with the sample. The difference of signal intensity as the beam passes through is detected and constructed into an ultra-high resolution image. All TEM bright field images were taken on a Gatan Tecnai TF20 TEM (FEI Inc.) operated at 200 keV. The lower magnification images show MOF particles are uniformly dispersed on LSG (Figures 4-2a & b). This observation is consistent with the SEM results.

After sonication and stirring, the prismatic crystals break down to particles with kinetically stable size and shape. As shown in Figure 4-2c, a particle size in the range of 15 nm to 100 nm is observed. Since the pore diameter of the MOF-74 is around 11 Å, the smallest particles will still contain open pores that are accessible to electrolyte. The very tiny particles with a few nanometers in diameter could be somewhat degraded metal centers from the MOFs or salt residues from the GO synthesis.

19
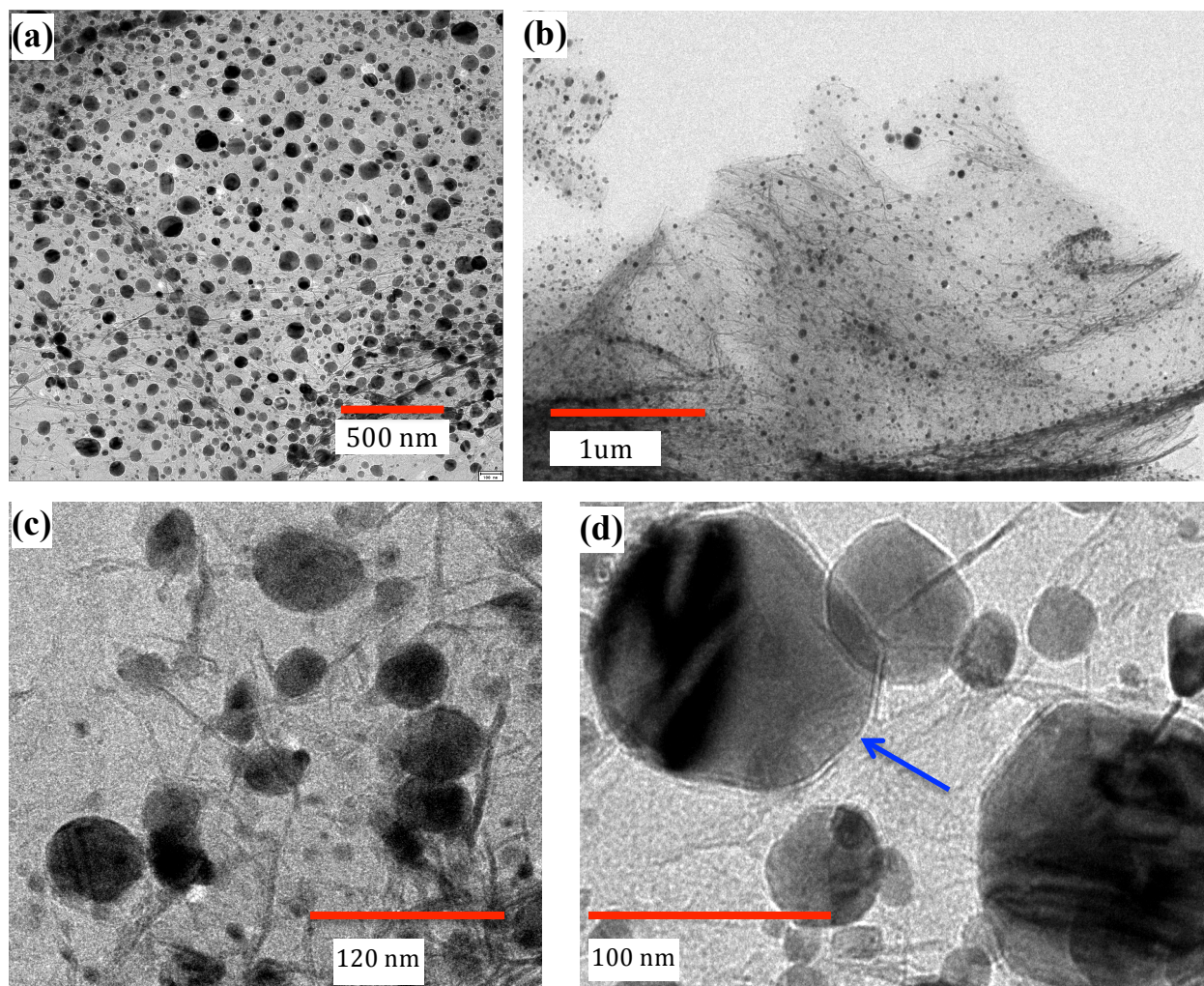
Figure 4-2. SEM images of MOF-74/LSG sample at different magnifications: (a) 19K, (b) 6.5K, (c) 50K, and (d) 80K. The blue arrow points at a MOF particle being wrapped by a graphene sheet.

Interestingly, the highest magnification (x 80K) image shows that the MOF particles are wrapped by graphene sheets, indicated by the blue arrow in Figure 4-2d. This remarkable observation validates the hypothesis of the strong interaction between MOFs and GO. More importantly, the graphene sheets can maintain the close interaction with MOFs even after laser irradiation. By tightly wrapping the MOF particles, LSG not only can protect MOFs from laser degradation, but also can efficiently transport the charges generated by MOFs out of their frameworks. This leads

20

to the excellent electron and proton conductivity of the MOF/LSG hybrid electrode reported later in this thesis.

4.3 X-Ray Photoelectron Spectroscopy (XPS)

X-Ray Photoelectron Spectroscopy (XPS) also known as Electron Spectroscopy for Chemical Analysis (ESCA) is widely used as a surface-sensitive quantitative spectroscopic technique. It can determine the elemental composition, chemical state, and electronic state of the elements within the material of interest, and provides valuable information about the material properties. All XPS spectra reported here were collected using a Kratos Axis Ultra DLD spectrometer equipped with a monochromatic Al K-alpha X-ray source, and high-resolution spectra were charge-corrected to a carbon 1s peak with a binding energy of 284.6 eV.

The XPS survey spectra display all the elements on the sample surface, which can be processed for subsequent high-resolution XPS spectra acquisition. The survey spectrum for LSG (Fig. 4-3a) shows a distinct carbon 1s (C 1s) peak and a low intensity oxygen 1s (O 1s) peak, indicating the reduction of GO. The complete reduction of GO is further confirmed by a close-up XPS spectrum of the C 1s envelope region (Fig. 4-4a), where only the sp^2 carbon photoemission peak at 284.0 eV and the sp^2 satellite peak from π-π* transition are present.[30] These peaks are the signatures of highly conductive carbon material. The survey spectra for M4M-MOF-74/GO and M4M-MOF-74/LSG spectra (Figs. 4-3b & 4-3c) contain all four metal photoemission peaks with corresponding binding energies as Co $2p_{3/2}$ at 780.6 eV and 780.3 eV, Ni $2p_{3/2}$ at 855.4 eV and 855.9 eV, Zn $2p_{3/2}$ at 1021.4 eV and 1021.8 eV, and Mg 1s at 1303.4 eV and 1304.1 eV, respectively. Minimal peak shifts are observed after laser scribing, which ensure the integrity of the MOF structure.

21

As expected, after the GO reduction, the intensity of the O 1s photoemission peak at 532.3 eV largely decreases (Figs. 4-3b and 4-3c), and the intensities of the metal peaks are systematically enhanced (Fig. 4-5). The reason is that the oxygenated functional groups in GO are reduced to carbon dioxide, and it results in oxygen signal intensity decline. Moreover, the percentage atomic composition of carbon has changed dramatically upon laser-scribing. The XPS spectrum of MOF/GO in the C 1s envelope region (Fig. 4-4b) shows 44.1% sp^2 carbon, 42.5% hydroxyl carbon (C-OH), 7.8% ether carbon (C-O-C), 4.8% carbonyl carbon (C=O), and 0.8% carboxyl carbon (COOH); this represents a typical carbon composition in GO. Amazingly, the 42.5% hydroxyl carbon intensity completely diminished after only two cycles of laser irradiation with 16% power. Since the C 1s peak for MOF/GO (Fig. 4-4c) is very similar to pure LSG carbon peak (Fig. 4-4a), it indicates the GO in MOF/GO film is fully reduced to the conductive LSG. Overall, the XPS spectra confirm that the laser irradiation can achieve sufficient GO reduction and enhance the intensities of all four metals of MOFs on the sample surface.
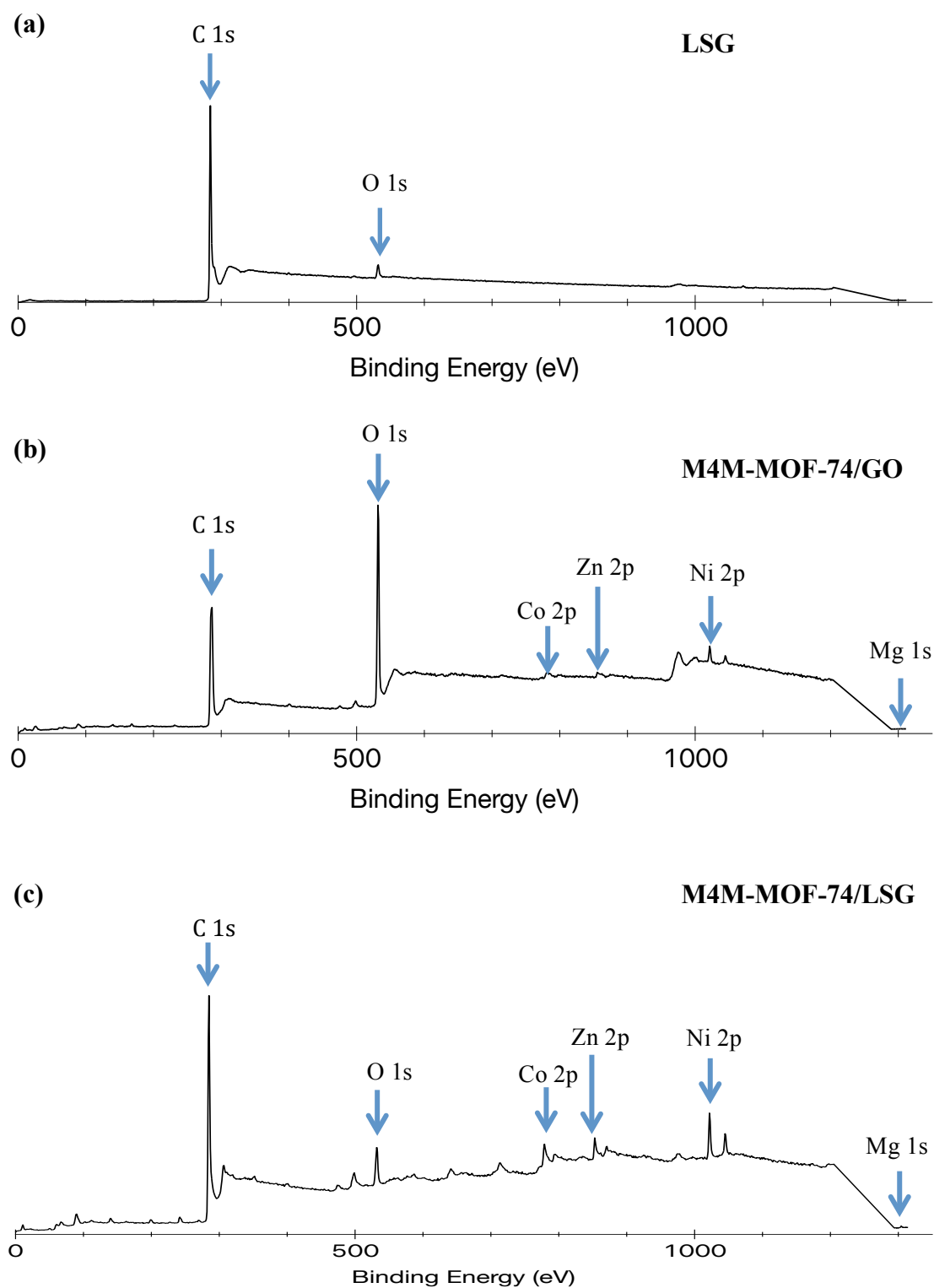
Figure 4-3. XPS survey spectra for (a) LSG, (b) MOF/GO and (c) MOF/LSG films. All four metal photoemission peaks from M4M-MOF-74 are observed, and the intensities of the metal peaks increased after laser irradiation.
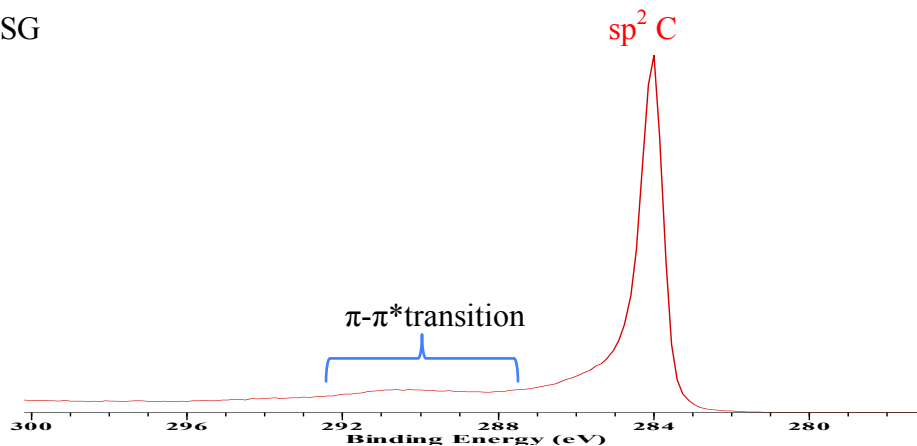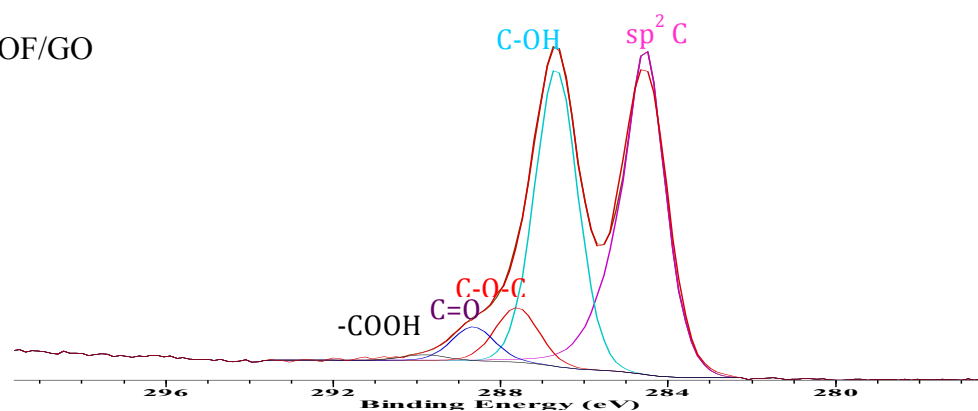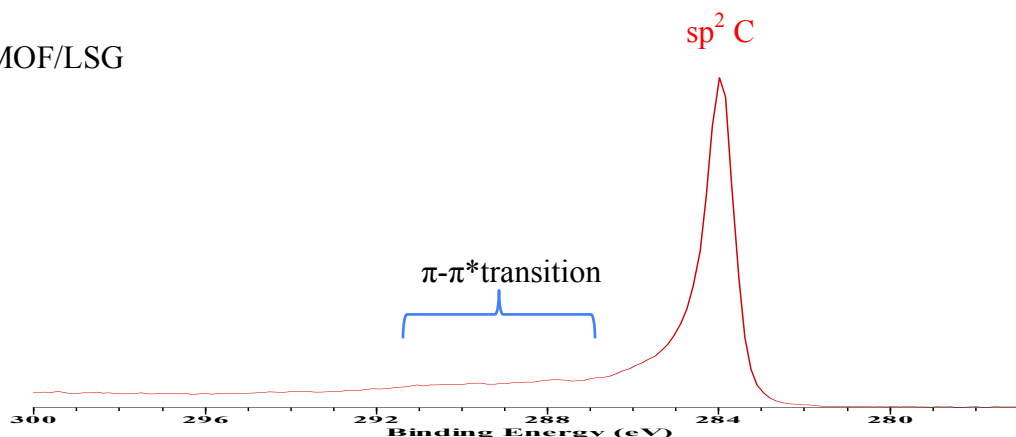
Figure 4-4. XPS spectra for carbon 1s envelope for (a) LSG, (b) M4M-MOF-74/GO and (c) M4M-MOF-74/LSG films. The sp^2 carbon photoemission peak at 284.0 eV and the sp^2 satellite peak from π-π* transition are present for LSG and MOF/LSG samples. Besides 44.1% sp^2 carbon, the MOF/GO spectrum also shows other carbon compositions, such as 42.5% hydroxyl carbon (C-OH), 7.8% ether carbon (C-O-C), 4.8% carbonyl carbon (C=O), and 0.8% carboxyl carbon (COOH).
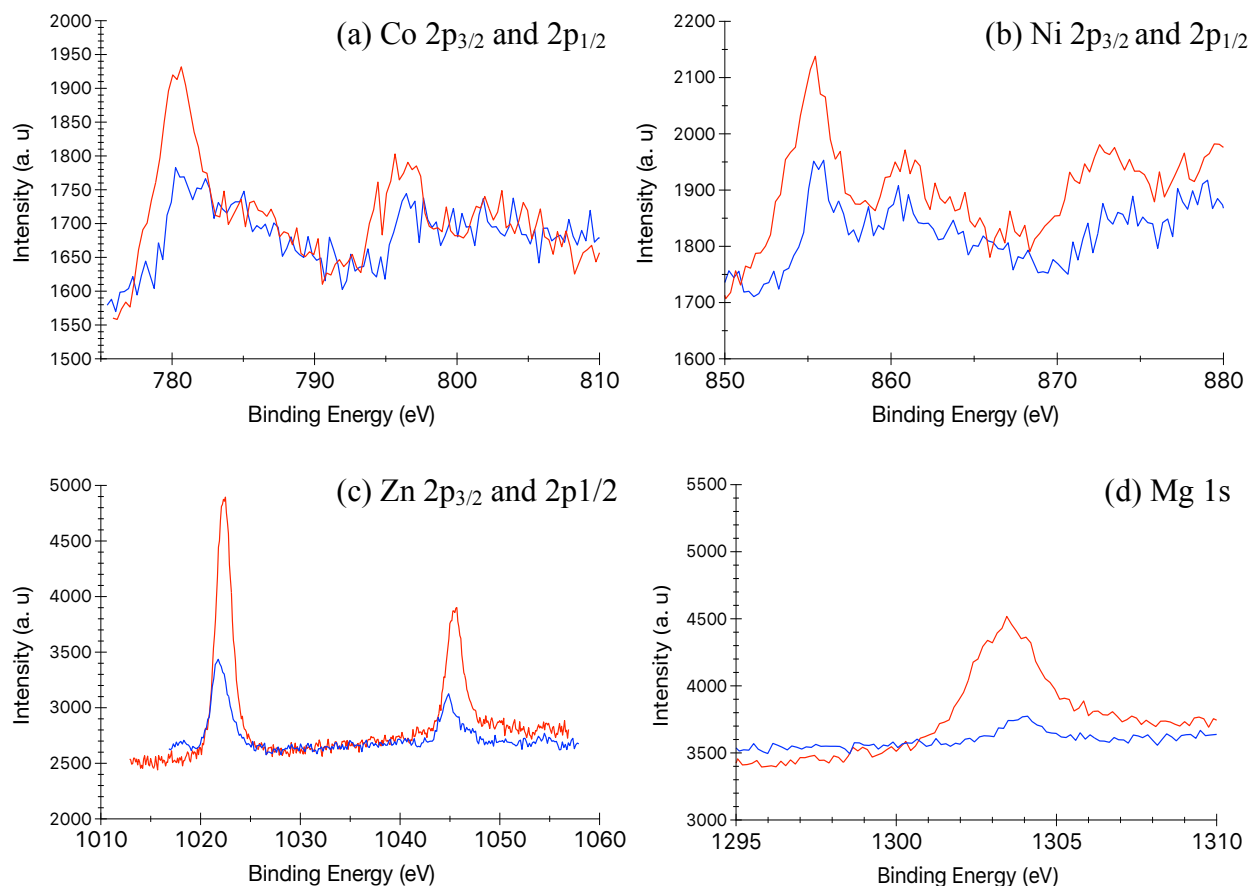
Figure 4-5. XPS spectra comparing M4M-MOF-74/GO (blue) and M4M-MOF-74/LSG (red) samples. The intensities of the photoemission peaks for (a) Co $2p_{3/2}$ and $2p_{1/2}$,(b) Ni $2p_{3/2}$ and $2p_{1/2}$,(c) Zn $2p_{3/2}$ and 2p1/, and (d) Mg 1s show systematic increase after GO reduction.

4.4 X-ray Diffraction (XRD)

A Bruker AXS D8 Advance diffractometer with CuKα radiation (λ = 1.5406 Å) that measures the crystal structure of powder and thin film materials was used to study the effect of the laser irradiation on the MOFs crystallinity. The diffraction patterns were processed using PANalytical X'Pert HighScore Plus. The M4M-MOF-74/GO and M4M-MOF-74/LSG samples appear to have relatively low signal-to-noise ratios, because the samples are self-standing thin films peeled off from the PET substrates. The XRD spectra measured for MOF/GO and MOF/LSG (Fig. 4-6) in a range of 2θ from 3° to 30° show diffraction peaks at 2θ = 9.65° for GO and 2θ = 25.57° for LSG,

25

respectively. This result is consistent with the literature[31], suggesting that the distances between graphene layers decrease as GO is being converted into LSG. Moreover, the two most distinct (110) and (300) reflection peaks of MOF-74 at a 2θ of 6.78° and 11.77°, respectively, are present in the MOF/GO and MOF/LSG spectra, which confirms the crystallinity of the M4M-MOF-74 before and after the laser-scribing GO reduction.
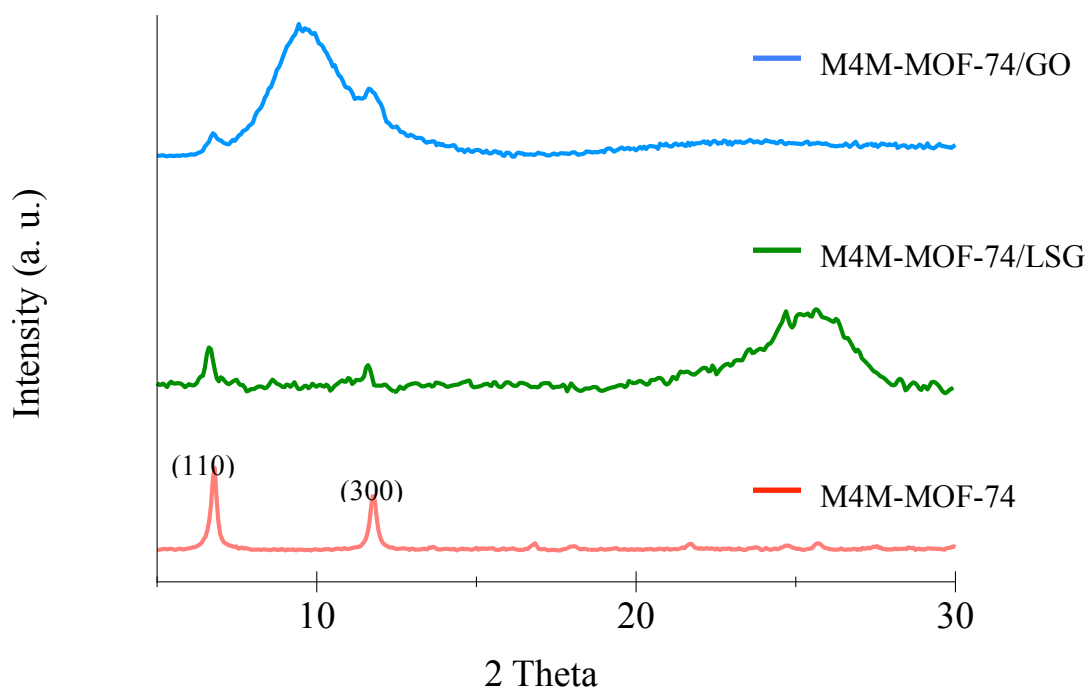
Figure 4-6. XRD patterns of M4M-MOF-74/GO and M4M-MOF-74/LSG comparing with pure M4M-MOF-74. M4M-MOF-74/GO and M4M-MOF-74/LSG samples have (110) and (300) reflection peaks from M4M-MOF-74. The GO (2θ = 9.65°) and graphene (2θ = 25.57°) peaks are observed in M4M-MOF-74/GO and M4M-MOF-74/LSG spectra, respectively.

Chapter 5: Electrochemical Measurements of M4M-MOF74/LSG Hybrid Electrodes

5.1 Three-electrode Measurements

The electrochemical properties of the M4M-MOF74/LSG electrodes were investigated in a conventional three-electrode setup using a platinum foil counter electrode and a Ag/AgCl reference electrode. As illustrated in Figure 5-1, the working electrode was prepared by applying silver paint around a desired area of the testing material (MOF-74/LSG on PET), connecting a piece of copper tape to the dried silver paint, and passivating the Ag paint and copper tape areas with Kapton tape. The exposed testing material was considered as the active material for areal and gravimetric capacitance measurements. Most analytical electrochemical experiments are only interested in the potential of the working electrode, which is the reason that the three-electrode configuration is commonly used. By introducing a reference electrode with a known reduction potential, one can monitor the current between the working and the counter electrodes, and the voltage between the reference and the working electrodes in such a setup (Fig. 5-2). All electrochemical date reported were collected by a VMP3 BioLogic Multi Potentiostat and processed using the EC-lab V10.23 program.
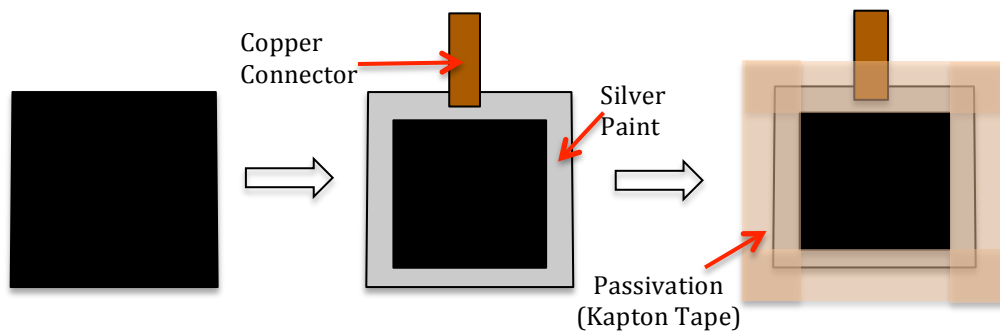
Figure 5-1. Assembly of a working electrode with testing material.
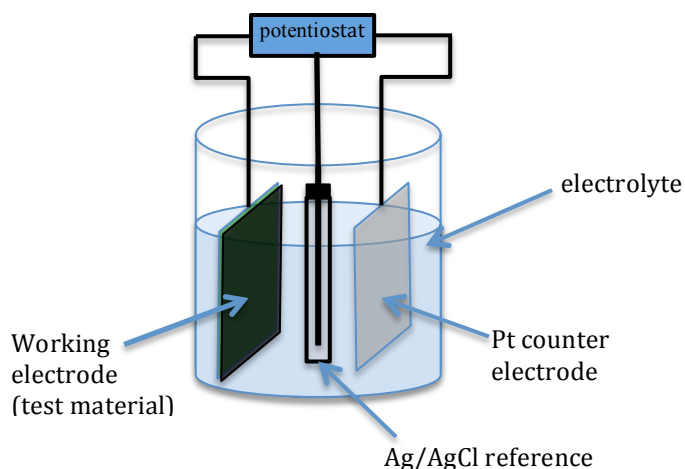
Figure 5-2. Schematic illustration of the three-electrode setup for electrochemical measurements. By employing a potentiostat, one can monitor the current between the working and the counter electrodes, and the voltage between the reference and the working electrodes in the three-electrode setup.

5.2 Cyclic Voltammetry (CV)

Cyclic voltammetry measurements were conducted to evaluate the charge storage behavior and determine the operating voltage of the M4M-MOF-74/LSG (referred as MOF/LSG for simplicity) electrodes in 1 M aqueous H_2SO_4 (Sigma-Aldrich) electrolyte. At a scan rate of 100 mV/s, the CV profile of the pure LSG electrode appears rectangular in shape, which suggests an ideal electric double-layer capacitor (EDLC) behavior. Whereas the CV profile of the MOF/LSG electrode combines the ideal rectangular shape with broad redox peaks (Fig. 5-3a), indicating the hydride electrode exhibits both electrostatic separation of charges and reversible Faradaic charge-transfer behaviors.

Generally, MOFs are considered as electrically insulating materials. Recent studies show that some MOFs exhibit excellent proton conductivity and have been developed in fuel cell applications.[32] Particularly, Phang et al. discovered the outstanding proton conductivity of Ni-MOF-74 under acidic conditions via the Grotthuss or proton-hopping mechanism.[33] The protons in H_2SO_4 electrolyte form H_3O^+ species within a water cluster; proton transfer occurs upon

28

severing of hydrogen-bonds, and subsequently transfer to nearby H_2O molecules.[32] The rectangular base of the MOF/LSG CV curve indicates good conductivity of the electrode material. Without using binders or conductive substrates, this result not only reveals the important role of graphene in enhancing the conductivity of the hybrid electrode, but also suggests that the acidified MOF further improves proton transport within the system.

The pronounced redox peaks in the CV curves greatly contribute to capacitance improvement. An average redox potential of 0.17 V is measured, where the oxidation and reduction occur at 0.26 V and 0.09 V (all vs. Ag/AgCl), respectively. Based on the observation of the shoulders on the large peaks, several redox peaks are possibly overlapped to give the high current density. As previously shown that LSG sheets maintain the physical contacts with MOF particles after laser reduction, the excellent charge transport from MOFs to LSG can cause the redox peaks to be less defined and allow the overall CV profile to be more rectangular. Additionally, the kinetic barriers, such as the diffusion of electrolyte to active material and electro-conductivity of the device, account for the small potential difference between the oxidization and reduction peaks, which is common in electrochemical devices.

It is also noteworthy that the maximum operating voltage is as large as 1.6 V in aqueous H_2SO_4 electrolyte (Figs. 5-3a and 5-4b). The MOF-74/LSG electrode does not experience a tendency to undergo hydrogen evolution in the applied voltage window, whereas the LSG electrode starts reaching hydrogen evolution at -0.5 V (vs Ag/AgCl). The wide potential window in MOF-74/LSG is presumably a result of the strong interaction between MOFs and LSG; followed by the reduction, MOF particles are well intercalated into the graphene sheets, the charges generated from redox reactions can be carried out by the conductive LSG, and attributed to the overall charge storage.

Most importantly, the MOF/LSG electrode demonstrates a significant increase in current density when compared to the pure LSG electrode (Fig 5-3); this result indicates that doping MOF-74 with the conductive LSG improves capacitance and enables MOFs to contribute to charge storage. Although MOFs are not known to exhibit pseudocapacitance, the MOF/LSG electrode holds reproducible and stable capacitive behavior as increasing scan rates up to 200 mV s^{-1} (Fig. 5-3b); specifically, the areas under the CV curves increase proportionally with the scan rate. At a scan rate of 100 mV s^{-1}, the MOF/LSG electrode obtains a high areal capacitance of 43.8 mF/cm^2, which is about four times higher than the capacitance of the LSG electrode, 11.3 mF/cm^2. This substantial improvement emerges from the Faradaic processes of MOFs combined with the highly conductive LSG to create a system with extraordinary surface area and 3-dimensional interconnected pores. These pores allow the protons to freely access the frameworks and interact with active site in the MOFs to undergo reversible redox processes.

(a) **(b)**
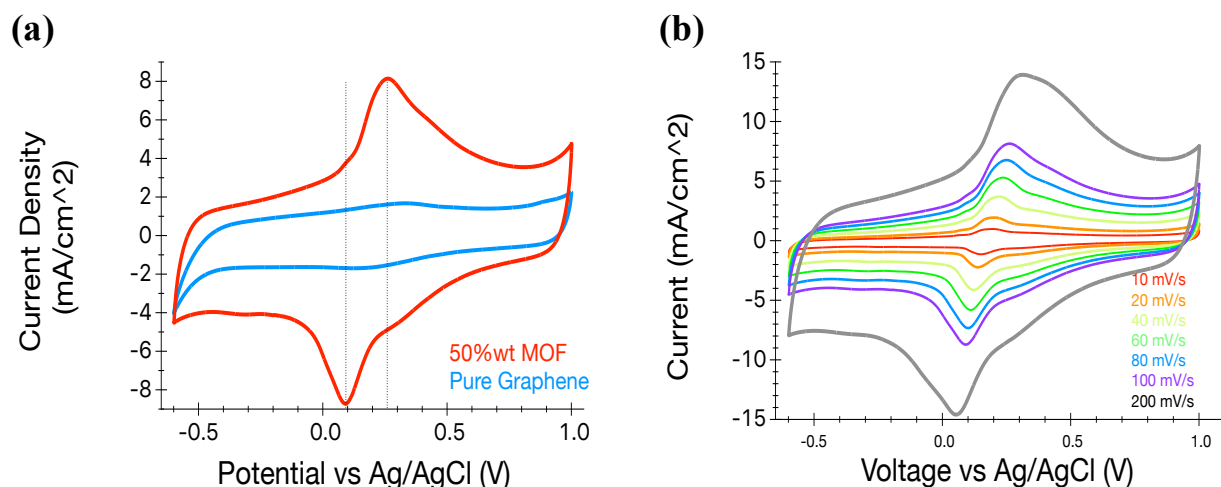
Figure 5-3. Cyclic voltammetric measurements of MOF-74/LSG and LSG electrode in 1M aquous H$_2$SO$_4$ electrolyte. (a) CV of MOF-74/LSG (red) and LSG (blue) obtained at 100 mV/s. (b) CV of MOF-74/LSG measured with scan rate at 10, 20, 40, 60, 80, 100, and 200mV/s.

5.3 Galvanostatic Charge/Discharge Measurements

Galvanostatic charge/discharge or constant current (CC) measurements were also performed to investigate the charge storage ability of the MOF/LSG hybrid electrode. Figure 5-4 displays the hybrid electrode response accordingly with increasing current density, demonstrating its excellent ability to uptake and store charge. When the supplied current density doubles, the time that the electrode takes to charge and then discharge is reduced by half. A small IR drop observed at the beginning of the discharge curve suggests low internal resistance of the electrode. Based on the CC data, the equivalent series resistance (ESR) is calculated to be 3.4 Ω cm^2. Thus, by incorporating MOFs with graphene the electrode preserves a minimal level of internal resistance. Furthermore, the shoulders on the CC curves correspond to the large redox peaks around 0.17 V (vs Ag/AgCl) observed in the CV data. The overall triangular shape of the charge/discharge curves validates the excellent capacitive behavior of the MOF/LSG electrodes.
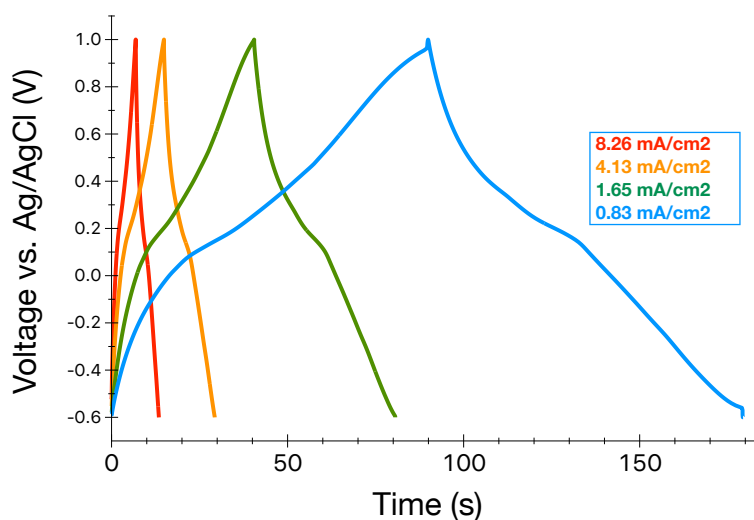
Figure 5-4. Galvanostatic charge/discharge (CC) of MOF/LSG electrode at various current densities, 0.83, 1.65, 4.13, and 8.26 mA cm^{-2}.

5.4 Electrochemical Impedance Spectroscopy (EIS)

Next, electrochemical impedance spectroscopy was conducted and the results are displayed in the form of Nyquist plots. In Figure 5-5, the Nyquist plot of the MOF/LSG electrode is compared with the LSG electrode plot to present their capacitive behaviors through impedance measurements. The steeply rising pattern of MOF/LSG in the low frequency region (Fig. 5-5) appears to be almost vertical, which reflects its superior capacitive behavior compared to the LSG electrode. The intercept of the Nyquist plot on the Z real axis for MOF/LSG is approximately 3.5 Ω cm^2 that confirms the good conductivity of the electrode. This value is consistent with the calculated ESR (3.4 Ω cm^2), showing the low internal resistance of the system. Even though Faradaic processes occur during the charge and discharge of the MOF/LSG electrode that are evidenced by the large redox peaks, there is a very small semi-circular arc in the high frequency region (Fig. 5-5b). This indicates the low charge transport resistance at the electrode/electrolyte interface and suggests fast and efficient charge propagation within the 3-dimensional porous MOF/LSG electrodes. Even with the absence of the high frequency semi-circular arc, the ion transport within the LSG electrode is not nearly as favorable as in the MOF/LSG, verified by the less vertical rising of the impedance curve as the frequency drops. Since the Z real axis intercept of LSG electrode is 10.9 Ω cm^2, the internal resistance is higher in comparison with the MOF/LSG system.
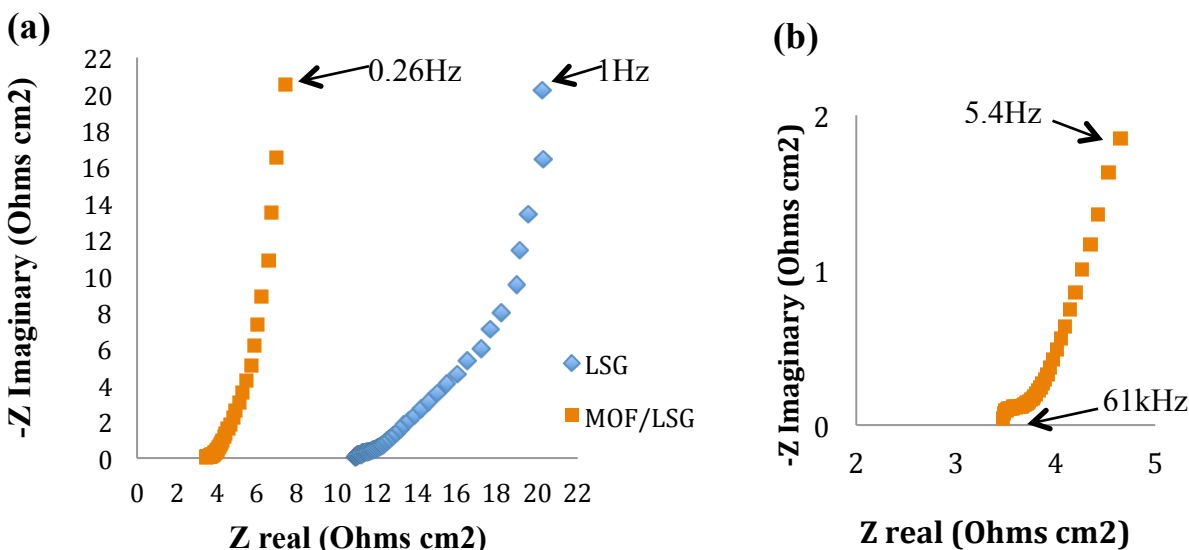
Figure 5-5. Nyquist plot of (a) MOF/LSG electrode comparing with LSG electrode and (b) MOF/LSG electrode in the high frequency region.

5.5 Rate retention

Moreover, the rate capability of the MOF/LSG electrode was investigated. Figure 5-6 presents the remarkable areal capacitance retention of MOF/LSG, by the reason of rapid charge transport and low internal resistance within the system (Figure 5-6). The areal capacitance of the MOF/LSG electrode is consistently greater than the LSG capacitance as increasing the supplied scan rate. Even at a high scan rate of 400 mV/s, the MOF/LSG electrode obtains an areal capacitance of 36.4 mF/cm that is still 3.8 times higher than the LSG capacitance of 9.6 mF/cm. This confirms that the high porous and conductive electrode material enables the rapid ion and electron transport to improve capacitance.
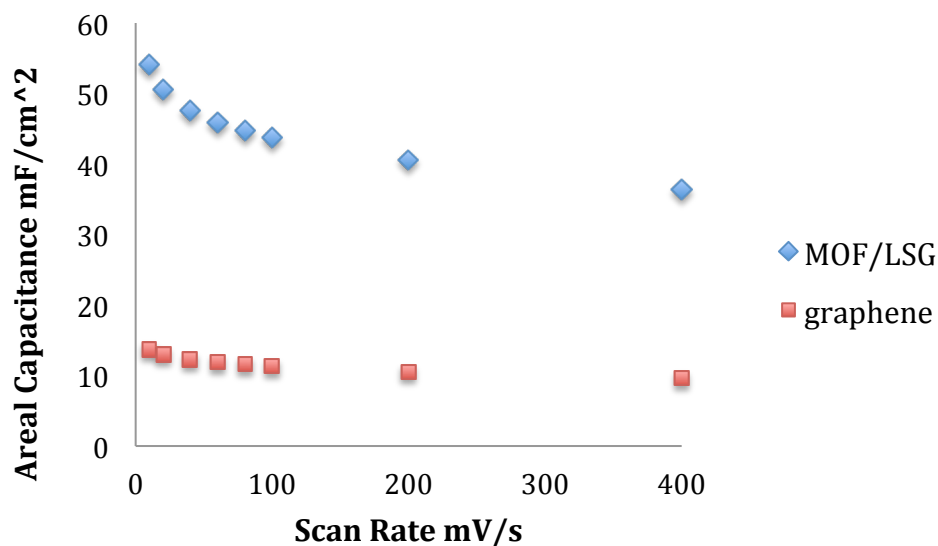
Figure 5-6. The areal capacitance retention of LSG and MOF/LSG electrodes as a function of scan rate.

5.6 Effect of Ion Size in Electrolytes

As previously mentioned, the highly conductive MOF/LSG electrode exhibits both EDLC behavior and Faradic processes in 1.0 M aqueous H_2SO_4 electrolyte, which give rise to an incredible improvement in areal capacitance. It is believed that the open and porous structure of the MOF/LSG complexes facilitates electrolyte infiltration, allows the small protons to freely transport through the active material, and thus enhancing the capacitance. For this reason, the effect of electrolytes with larger alkali metal ions on the MOF/LSG electrodes capacitance was explored. Figure 5-6b,c present the CV curves of MOF/LSG electrodes at 100 mV/s in 1.0 M $LiNO_4$ and 1.0 M Na_2SO_4 aqueous electrolytes, respectively. Considering the semi-rectangular shaped CV curves have no distinguishable redox peaks, the electrochemical reaction for MOF/LSG electrode in both $LiNO_4$ and Na_2SO_4 electrolytes can be defined as electro-adsorption.
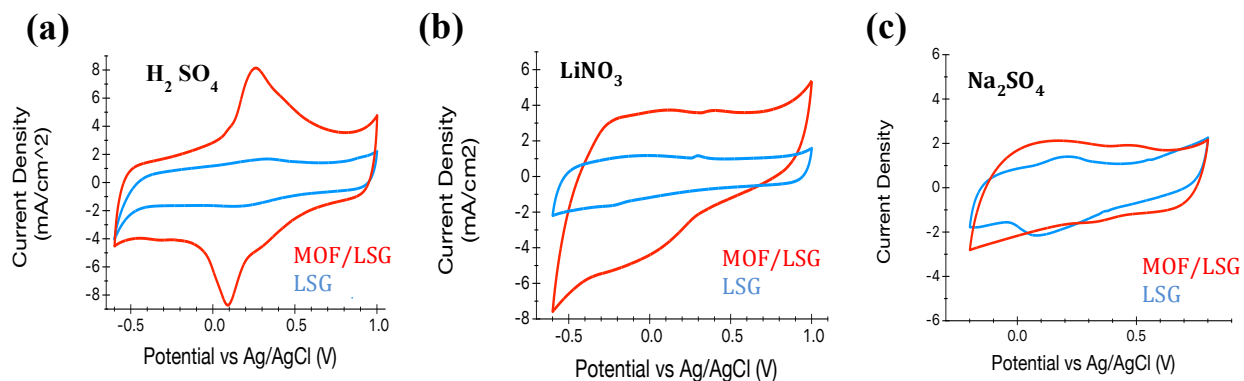
Figure 5-7. CV curves of MOF/LSG and LSG electrodes at 100mV/s in various aqueous electrolytes: (a) H_2SO_4, (b) $LiNO_3$ and (c) Na_2SO_4.

It is commonly known that alkali metal ions are strongly solvated in water solution, causing an increase of the ion-solvent complex diameter in the following: Li^+ (d = 3.81 Å) >Na^+ (d = 3.59 Å); also, the larger the ion-solvent complex diameter is, the lower the ion mobility and diffusion coefficient become.[34] However, when the porous materials on the electrodes are well saturated by the electrolyte, the ions are closely located by the electrode/electrolyte interface and can conveniently interact with the electrode over a short distance. Hence, for a simple ion adsorption, the ion-solvent complexes are not required to have a very high mobility to obtain the EDLC behavior. A study[34] shows that the best capacitive performance via electro-adsorption is obtained when the size of ion-solvent complex matches with the pore size of the electrode material. This could be the reason that the capacitance for MOF/LSG is higher in $LiNO_3$ electrolyte than in Na_2SO_4 electrolyte.

Moreover, the rate retentions of the MOF/LSG electrode in all three electrolytes are plotted in Fig. 5-7. After the initial increase in scan rate, a rapid capacitance decline occurs for $LiNO_3$ electrolyte system, possibly due to the low mobility of solvated Li^+ ion. At a relatively slow scan rate, the solvated ions are close to the electrode/electrolyte interface and can undergo the

electrostatic charge separation processes in a timely manner. In contrast, the low mobility of the solvated ion can largely delay the ion transport at a fast scan rate; thus, the capacitance drops dramatically.

Even though the size of the solvated cations can influence capacitance, the MOF/LSG electrodes still have better capacitive performance in all three electrolytes than the best-performing LSG electrode. This validates the importance of doping MOFs with graphene to fabricate more capacitive hybrid electrodes. Conclusively, operating the MOF/LSG in the H_2SO_4 electrolyte gives a significantly higher areal capacitance and the best rate capability over a large range of scan rates.
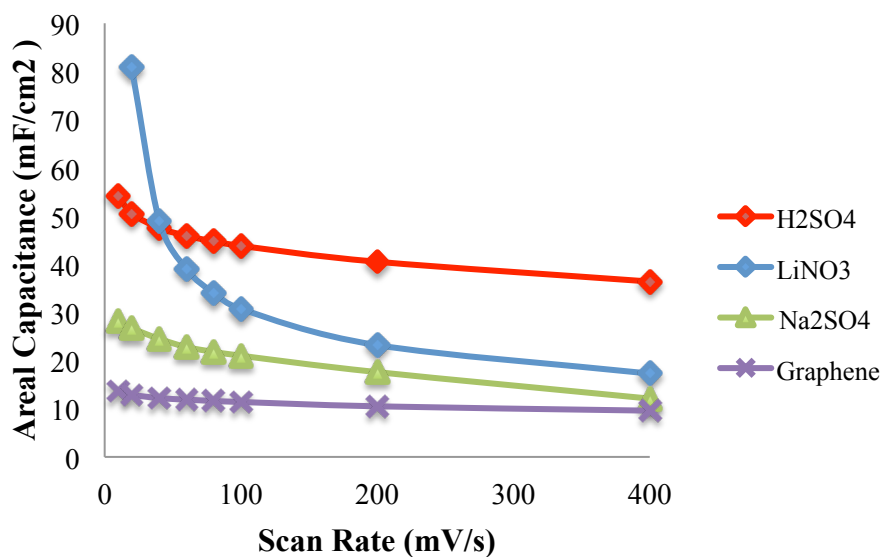

Figure 5-8. The areal capacitance retention of MOF/LSG electrode in various electrolytes as a function of scan rate. Areal capacitance calculated from the CV data of MOF/LSG collected in three aqueous electrolytes, H_2SO_4, $LiNO_3$ and Na_2SO_4. The real capacitance retention of LSG electrode was conducted in H_2SO_4 electrolyte.

Chapter 6: M4M-MOF74/Carbon Nanotubes Hybrid Electrodes

Another approach was taken by incorporating MOFs into conductive carbon nanotubes (CNTs) to further assess the capacitive behavior of M4M-MOF-74 and to evaluate the possible damage of the laser irradiation on the MOF structure. CNTs worked as fillers to form maximum conductive pathways within the MOF networks, and flash-reduced graphene (FRG) was used as fillers to further improve conductivity. Electrochemical measurements were conducted to compare with the electrodes fabricated by the laser scribing method.

6.1 Fabrication of M4M-MOF74/CNTs Hybrid Electrode

30 mg of M4M-MOF-74, 28.8 mg of commercially available single wall carbon nanotubes (SWCNTs) (Carbon Solutions Inc.), and 1.2 mg of flash-reduced graphene (FRG) were sonicated for 1 hour and then stirred for 30 minutes, both at 25°C. Freeze-dried graphene was reduced using an Alien Bees B1600 unit with a 7" diameter hemispherical reflector at full power (50-60 Hz). The MOF/CNTs/FRG mixture was drop cast on a 1.5 x 1.5 cm^2 piece of pre-weighted graphite paper (Digi-Key Electronics), and dried in room temperature overnight. The active material mixture with graphite paper was then assembled into an electrode with copper tape and passivated with Kapton tape.

6.2 X-ray Powder Diffraction (XRD) Characterization

The MOF/CNTs/FRG mixture was drop-cast onto a glass substrate for XRD characterization, which was performed using a Bruker AXS D8 Advance diffractometer with Cu Kα radiation (λ = 1.5406 Å). The diffraction patterns were processed by PANalytical X'Pert HighScore Plus. Figure 6-1 presents the XRD spectra for the active material of the MOF/CNTs/FRG electrode,

purchased CNTs, and M4M-MOF-74 in the range of 2θ from 3° to 60°. The two distinct (110) and (300) reflection peaks of MOF-74 at a 2θ of 6.78° and 11.77° are present in Figure 6-1a, which verify the crystallinity of MOF-74 (Fig. 6-1c) within the MOF/CNTs/FRG electrode. Besides the (002) and (101) reflection peaks of the CNTs in Figure 6-1b, there are three additional diffraction peaks that could be evidence for impurities. All diffraction peaks from the MOF/CNTs/FRG spectrum either correspond to MOF-74 or the peaks observed for the purchased CNT sample.
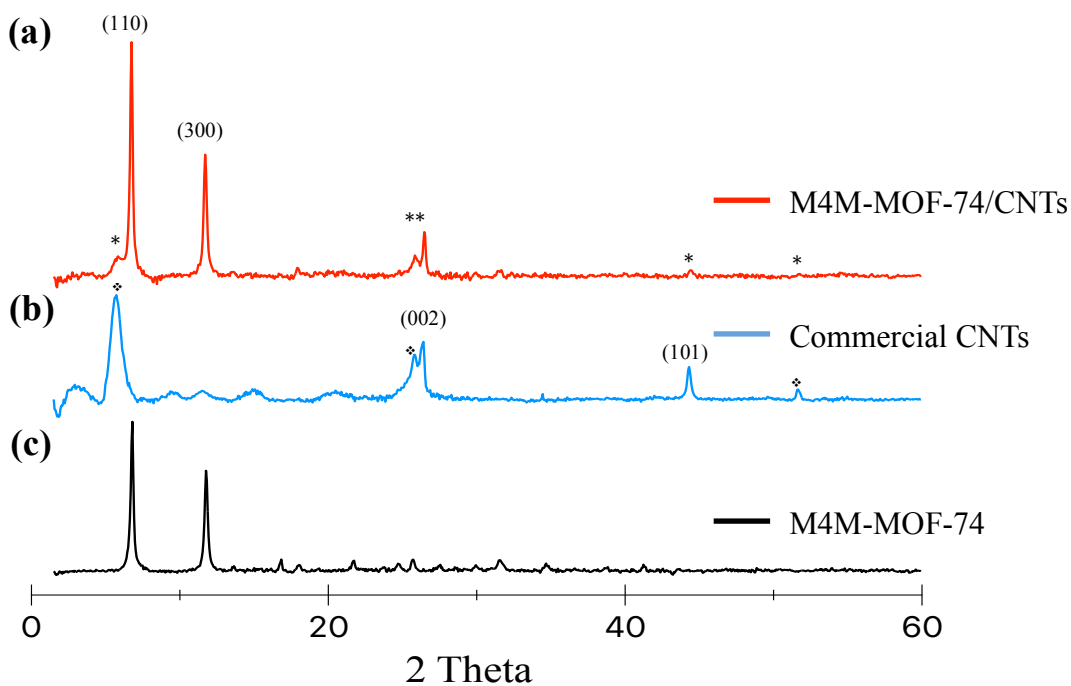

Figure 6-1. XRD spectrum of (a) the active material for the M4M-MOF-74/CNTs/FRG electrode, (b) commercially available CNTs, and (c) M4M-MOF-74. The XRD spectra measured in a range of 2θ from 3° to 60°. The impurities in the purchased CNTs are marked with "v". All CNTs peaks that are present in the M4M-MOF-74/CNTs/FRG sample are marked with "*".

6.3 Electrochemical Measurements

The electrochemical properties of the MOF/CNTs/FRG electrodes were also evaluated using a three-electrode configuration in 1 M aqueous H_2SO_4 electrolyte. As shown in Figure 6-2a, the CV profiles demonstrate a combination of both EDLC behavior and distinct redox processes. The largest redox peaks center at 0.16 V, where the oxidation occurs and 0.22 V and reduction occurs at 0.10 V (all vs. Ag/AgCl); these are consistent with the MOF/LSG results. The CV data also suggest great capacitive behavior of the electrode as the CV curves increase proportionally in area with the scan rate.

Note that the redox peaks for the MOF/CNTs/FRG electrodes are more defined than the ones for the MOF/LSG electrodes. There could be two possible reasons for this observation. First, some degree of degradation occurs to the MOF structures during laser irradiation. Second, CNTs do not make very good physical contacts with the MOF particles, whereas LSG sheets are able to wrap around the MOFs (Fig. 6-2). The excellent charge transport from MOFs to LSG allows the overall CV profile to be more rectangular, and the less sufficient charge transport leaves the redox peaks of the MOFs in MOF/CNTs/FRG electrodes to be more defined.

It is also worth noticing that the maximum voltage window for the MOF/CNTs/FRG electrode is 0.9 V, which is 0.7 V less than the MOF/LSG electrode. The efficient charge transport between MOFs and LSG conceivably enlarges the operating voltage window as well; hence, combining MOF and GO can better enhance proton and electron conductivity of the electrode, and improve the overall electrochemical performance.
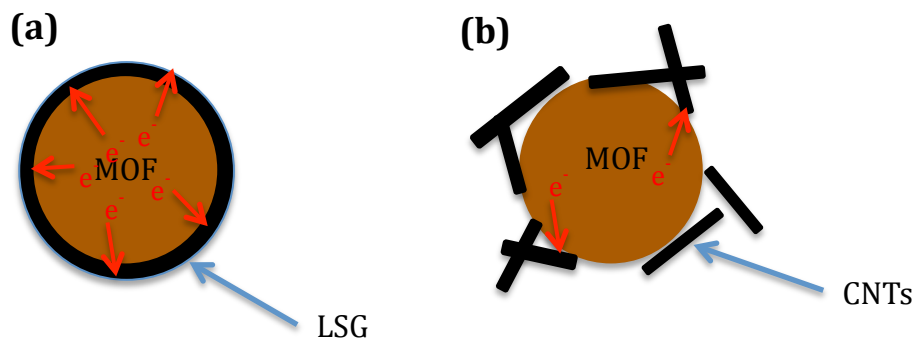
Figure 6-2. Predicted models to illustrate (a) the interaction between MOF particles and LSG and (b) interaction between MOF particles and CNTs. (a) Shows that when the LSG wraps the MOF particles after laser irradiation, a high efficiency of charge transport occurs in the MOF/LSG complexes, and (b) CNTs form conductive pathways around the MOF particles, but their interaction with MOFs and the charge transport are less favorable.

Likewise, the CC curves validate the excellent capacitive behavior of the MOF/CNTs/FRG electrode (Fig. 6-3b). The charge/discharge time integral decreases with increasing the supplied current density. As previously seen, the shoulders on the CC curves correspond to the large redox peaks in the CV data. The minimal IR drop is indicative of the low internal resistance within the electrode. Moreover, the Nyquist plot of the MOF/CNTs/FRG electrode is displayed in Figure 6-3c to compare with the MOF/LSG electrode. Although the MOF/CNTs/FRG electrode was prepared using a conductive substrate, the lower value of the intercept of the Nyquist plots on the real axis reveals that the MOF/LSG electrode obtains better conductivity and lower internal resistance for the system. The small semi-circular resistances in the high frequency region for both electrodes verify the low charge transfer resistance at the electrode/electrolyte interface and suggest favorable ion transport within the 3-dimensional porous networks. Finally, both areal capacitance retention plots show ideal capacitive behavior of the electrode materials, where the capacitance does not experience a significant drop as the scan rate is increased. Based on the results above, not only does incorporating MOFs into the

carbon-based electrodes not sacrifice the electrode conductivity, but this can also substantially enhance the overall capacitance of the electrodes.

(a)

(b)

(c)

(d)
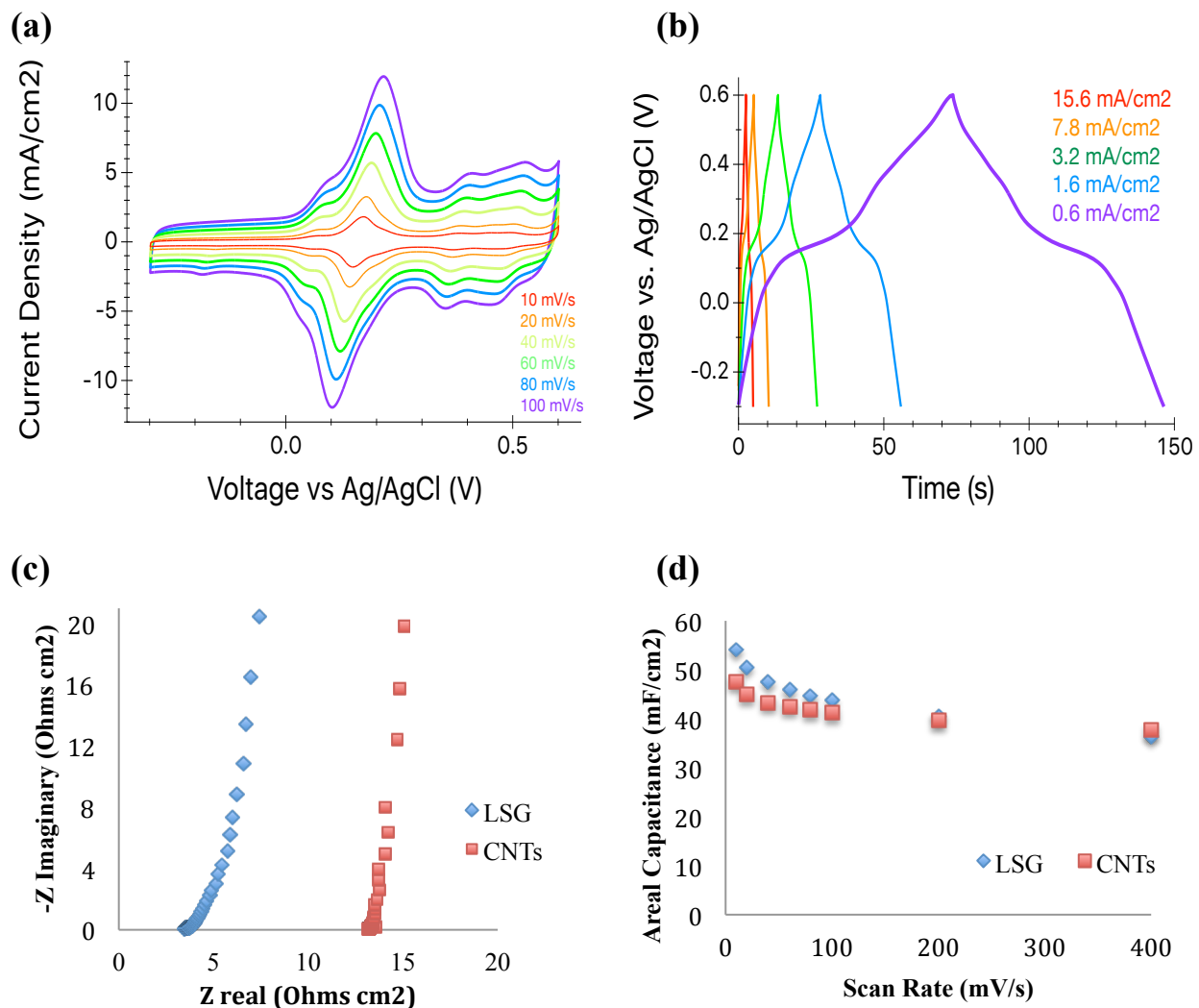
Figure 6-3. Electrochemical measurements for MOF/CNTs/FRG electrode in 1M aqueous H_2SO_4 electrolyte. (a) Cyclic voltammetry measurements with scan rate of 10, 20, 40, 60, 80, and 100 mV/s. (b) Galvanostatic charge/discharge at various current densities, 0.6, 1.6, 3.2, 7.8, and 15.6 mA cm^{-2}. (c) Nyquist plot of MOF/LSG electrode and MOF/CNTs/FRG electrode. (d) Areal capacitance retention of MOF/LSG and MOF/CNTs/FRG electrode electrodes as a function of scan rate.

Chapter 7: Conclusions

7.1 Summary and Findings

In summary, a simple and efficient laser irradiation method was employed to fabricate the highly capacitive M4M-MOF-74/LSG hydride electrodes, which exhibit both electrostatic separation of charges and reversible Faradaic charge-transfer behaviors. By combining MOFs with the highly conductive LSG, we created a system with extraordinary surface area and three-dimensional interconnected pores. These pores allow the protons to freely access the frameworks and interact with active site in MOFs to undergo the reversible redox processes. The favorable interaction between MOFs and GO is maintained even after the laser irradiation, in which LSG sheets tightly wrap around the MOF particles as observed in TEM images. This not only improves the electron conductivity of the electrode, but also preferentially helps transport the charges generated by the Faradaic processes in the MOFs. At a scan rate of 10 mV s^{-1} in 1 M H$_2$SO$_4$ aqueous electrolyte, the MOF/LSG electrode obtain a high areal capacitance (54.1 mF/cm^2) that is about four time higher than the capacitance of the pure LSG electrode (13.7 mF/cm^2). Moreover, the hybrid electrodes show excellent rate capability with an areal capacitance retention of approximately 67.3% when the scan rate increased from 10 mV/s to 400 mV/s. These results demonstrate that when doped with graphene, the ion adsorption, proton conductivity and Faradaic charge transfer properties of M4M-MOF-74 enable its ability to contribute to capacitance. Therefore, this work provides new understandings on potential applications of MOFs in electrochemical capacitors.

7.2 Future Directions

In order to incorporate the hybrid electrode in real-life devices, two-electrode measurements must be conducted. Both symmetric and asymmetric M4M-MOF-74/LSG hybrid supercapacitors need to be evaluated for electrochemical performance. In a symmetric electrochemical capacitor, two MOF/LSG electrodes of identical active areas are assembled with a separator inserted between the two electrodes. On the other hand, in an asymmetric system, an activated carbon negative electrode can be paired with the MOF/LSG positive electrode. The preliminary results show that the MOF/LSG electrodes preform better using the asymmetric system. To optimize the performance, the composition of the activated carbon negative electrode needs to be further studied, which may require certain levels of additives, such as binders or carbon black, to be compatible with the MOF/LSG electrode. Furthermore, the electrochemical performance of the MOF/LSG supercapacitors needs to be characterized by electrochemical impedance spectroscopy, cyclic voltammetry, and galvanostatic charge/discharge measurements. Finally, by assembling the hybrid electrodes into two-electrode devices, we can properly assess the stack capacitance, thus accurately measuring the energy and power densities of these supercapacitors. Based on this study, these devices are expected to have low internal resistance, high stack capacitance, and long cycling life, which could offer a promising energy storage solution for next generation electronics.

REFERENCE

(1)   Zhao, X.; Sanchez, B. M.; Dobson, P. J.; Grant, P. S. *Nanoscale* **2011**, 3, 839.

(2)   A Sustainable Solution for Public Transportation. Retrieved from http://www.sinautecus.com/products.html.

(3)   Lu, R.; Zhu, C.; Tian, L.; Wang, Q. *IEEE Transactions on Magnetics* **2007**, 43, 254-258.

(4)   Chen, J. ; Jang C.; Xiao, S.; Ishigami M.; Fuhrer M. *Nature Nanotech.* **2008**, 206 (3), 206-209.

(5)   Ghosh, A.; Subrahmanyam, K. S.; Krishna, K. *J. Phy Chem C* **2008,** 112 (40), 15704–15707.

(6)   El-Kady, M. F.; Strong, V.; Dubin, S.; Kaner, R. B. *Science* **2012**, 335, 1326.

(7)   Zhang, L.L; Zhao, X. S. *Chem. Soc. Rev.* **2009**, 38, 2520–2531.

(8)   Chen, T. ; Dai, L. *Materials Today* **2013**, 16(7-8), 272-280.

(9)   Cheng, Q.; Tang, J.; Ma, J.; Zhang, H.; Shinya, N.; Qin, L. *Carbon* **2011,** 49, 2917-2925.

(10)   Hu; G., Tang, C.; Li, C.; Li, H.; Wang, Y.; Gong, H. *J. Electrochem. Soc.* **2011**, 158, A695.

(11)   Brousse, T.; Be ́langer, D.; Long, J. W. *J. Electrochem. Soc.* **2015,** 162 (5), A5185-A5189.

(12)   Hwang, J. Y; El-Kady, M.F.; Wang, Y.; Wang, L.; Shao, Y.; Marsh, K.; Ko, J.M.; Kaner, R. B. *Nano Energy* **2015**, 18, 57–70.

(13)   Brousse, T.; Toupin, M.; Dugas, R.; Athoue ̈l, L.; Crosnier, O.; Be ́langer, D.; *J. Electrochem. Soc.* **2006**, 153, A2171.

(14)   Yaghi, O. M.; Li, H.. *J. Am. Chem. Soc.* **1995**, 117 (41), 10401–10402.

(15)   Cook, T. R.; Zheng, Y.; Stang, P.J. *Chem Rev.* **2013**, 113(1), 734–777.

(16)   Zhou, H.; Long, J.; Yaghi O.M. *Chem Rev.* **2012**, 112, 673-674.

(17)   Furukawa, H., Cordova, K. E.; O'Keeffe, M.; Yaghi, O. M. *Science* **2013**, 341, 1230444.

(18)   Usman, M.; Mendiratta, S.; Batjargal, S.; Haider, G.; Hayashi, M.; Gade, N. R.; Chen, J.; Chen, Y.; Lu. K.. *ACS Appl. Mater. Interfaces* **2015**, 7, 22767−22774.

(19)   Stavila, V.; Talin, A. A.; Allendorf, M. D. *Chem. Soc. Rev.* **2014**, 43, 5994–6010.

(20)   Choi, K. M; Jeong, H. M.; Park, J. H.; Zhang, Y.; Kang, J. K.; Yaghi, O.M. *ACS Nano*. **2014**, 8(7), 7451-7457.

(21)   Chmiola, J.; Largeot, C.; Taberna, P.L.; Simon, P.; Gogotsi, Y. *Angewandte Chemie International Edition* **2008**, 47, 3392–3395.

(22)   Glover, T. G.; Peterson, G. W.; Schindler, B. J.; Britt, D.; Yaghi, O. M. *Chemical Engineering Science* **2011,** 66, 163−170.

(23)   Peterson, G. W.; Mahle, J.; Balboa, A.; Wagner, G.; Sewell, T.; Karwacki, C. J. Evaluation of MOF-74, MOF-177, and ZIF-8 for the Removal of Toxic Industrial Chemicals; Edgewood Chemical Biological Center, U.S. Army Research, Development and Engineering Command: Aberdeen Proving Ground, MD, 2008.

(24)   Wang, L. J.; Deng, H.; Furukawa, H.; Gańdara, F.;.Cordova, K. E.; Peri, D.; Yaghi, O.M. *Inorg. Chem.* **2014**, 53 (12), 5881–5883.

(25)   Millward, A. R.; Yaghi, O. M. *J. Am. Chem. Soc.* **2005**, 127 (51), 17998–17999.

(26)   Cho, H.; Yang, D.; Kim, J.; Jeong, S.; Ahn, W; *Catalysis Today* **2012,** 185(1), 35–40.

(27)   El-Kady, M. F.; Strong, V.; Dubin, S.; Kaner, R. B. *Science* **2012**, 335, 1326-1330.

(28)   Gilje, S.; Han, S.; Wang, M.; Wang, K. L.; Kaner, R. B. *Nano Lett.* **2007**, 7 (11), 3394–3398.

(29)   Full Spectrum LASER LLV V0.85 40W Hobby CO2 Laser Engraver Setup and Installation Guide. Retrieved from https://fslaser.com/Manuals/FSL_40w_Hobby_Laser_Manual.pdf

(30)   Jackson, S. T.; Nuzzo, R. G. *Applied Surface Science* **1995**, 90, 195-203.

(31)   Stobinski, L.; Lesiak, B.; Malolepszy, A.; Mazurkiewicz, M.; Mierzwa, B.; Zemek, J.; Jiricek, P; Bieloshapka, I. *Journal of Electron Spectroscopy and Related Phenomena*. **2014,** 195, 145-154.

(32)   Ramaswamy, P.; Wong, N. E.; Shimizu, G. K. *Chem. Soc. Rev.* **2014**, 43, 5913-5932.

(33)   Phang, W. J.; Lee, W. R.; Yoo, K.; Ryu, D. W.; Kim, B. S.; Hong, C. S. *Angew. Chem. Int. Ed.* **2014**, 53, 8383 −8387.

(34)   Fic, K.; Lota, G.; Meller, M.; Frackowiak, E. *Energy Environ. Sci*. **2012**, 5, 5842

(35)   Yang, J.; Zheng, C.; Xiong, P.; Lia, Y.; Wei, M. *J. Mater. Chem. A* **2014**, 2, 19005

(36)   Li, Y.; Feng, L.; Shi, X.; Wang, X; Yang, Y; Yang, K.; Liu, T.; Yang, G.; Liu, Z. *Small* 2014, 10 (8), 1544-1554.